MECHANICAL ENGINEERING DEPARTMENT

SCHOOL OF ENGINEERING
THE UNIVERSITY OF CONNECTICUT

STORRS, CONNECTICUT

TURBINE ENDWALL TWO-CYLINDER PROGRAM

Semi-Annual Status Report

Grant No. NSG 3238

January 1, 1980 - July 1, 1980

Submitted to:

Lewis Research Center

National Aeronautics and Space Administration
21000 Brookpark Road
Cleveland, Ohio 44135

Principal Investigator:

Lee S. Langston
Associate Professor
Department of Mechanical Engineering
University of Connecticut
Storrs, Connecticut 06268

Introduction

The following is a report of progress made during the third six-month period (January 1, 1980 to July 1, 1980) under NASA Grant No. NSG 3238, "Turbine Endwall Two-Cylinder Program." Under this grant an analysis and a series of experiments are being carried out to study the three-dimensional separation of fluid flow around two isolated cylinders mounted on an endwall.

The work reported comes under Task I and Task II of the program, and deals with:

a) water tunnel testing

b) wind tunnel construction and assembly

c) wind tunnel testing

d) model design and construction

e) analytical work

f) overview of program.

Water Tunnel Testing

Water tunnel testing began upon receipt and installation of the turbulence manipulators discussed in the last progress report[1].

I. Bulk Flow Properties

Using the hydrogen bubble generator (which is discussed in detail in Appendix A) the test section flow was checked for uniformity and a visual measurement of turbulence level was obtained. It was found that immediately after the perforated plate and screening was installed, the test section flow was steady and uniform. However, as testing time accumulated the plate and screening became dirty and instabilities began to appear in the test section flow. Dealing with this dirt problem requires constant disassembling

of the tunnel and cleaning of the turbulence manipulators. Testing at low test-section velocities ($V < .15$ ft/sec) minimizes the instability problem.

II. Main Stream Velocity and Boundary Layer Thickness Measurements

An unsuccessful attempt was made to measure these low flow velocities with a pitot static probe. First, and obviously, the very low dynamic heads available for measurement are a problem, and second, we may have run into some minimum Reynolds number restrictions associated with our particular probe, as discussed by Bradshaw[2]. At present, the bulk fluid velocity is measured using the hydrogen bubble generator and a strobe operating at an equal and known pulsing frequency to obtain a time scale and two fixed points in the flow field to obtain a length scale. This method works well with velocities as low as $V \approx 0.01$ ft/sec.

One of the best methods available for obtaining a velocity profile in the boundary layer is the use of a hot-wire anemometer. We have calibrated a hot-wire anemometer system in the tunnel free stream using the previously discussed method for velocity measurement. Using this calibration we take our hot-wire probe into the boundary layer to obtain a velocity profile. However, the hot-wire probe used is not temperature compensated and therefore drifts slowly as the water changes temperature. At present, for each velocity profile measured, an independent free stream velocity measurement is made using the hydrogen bubble method. We then offset the velocity profile given by the anemometer by an amount equal to the difference between its free stream velocity measurement and the bubble measurement. For this to be valid the anemometer output variation must be linear with temperature.

It was very quickly realized that a good definition of boundary layer thickness is hard to make when interpreting data with some scatter (see Figure 1) as well as data where the profile shape changes with test section velocity. Clearly, boundary layer thickness alone is not an adequate description of what is happening in our boundary layer. More information is given by a shape factor with main stream velocity calibration. It was found that the boundary layer changes as the upstream turbulence manipulators become dirty. In order to categorize boundary layer properties we have found it necessary to supply a velocity profile along with each set of data taken. Figure 1 shows velocity profiles at three different main stream velocities. Over the range of velocities 0.01 - 0.2 ft/sec., we have the following ranges of boundary layer thickness, displacement thickness, momentum thickness, and shape factor:

δ : .9 - 1.6 in.

δ^* : .011 - 0.051 in.

θ : .007 - 0.012 in.

H : 1.64 - 3.93

III. Saddle Point Data

Figure 2 shows a plot of saddle point location using the coordinate system given in the first progress report[3]. This data was all taken at a Reynolds number based on cylinder diameter of Re_d = 1203 while the cylinder spacing was first decreased (closing cylinders) and then increased (opening cylinders). Dye was injected onto the test section floor through both a probe and the dye injection sites in the floor. A polaroid picture was taken of the limiting streamline pattern and the saddle point locations were taken from the picture using the dye injection sites as a coordinate

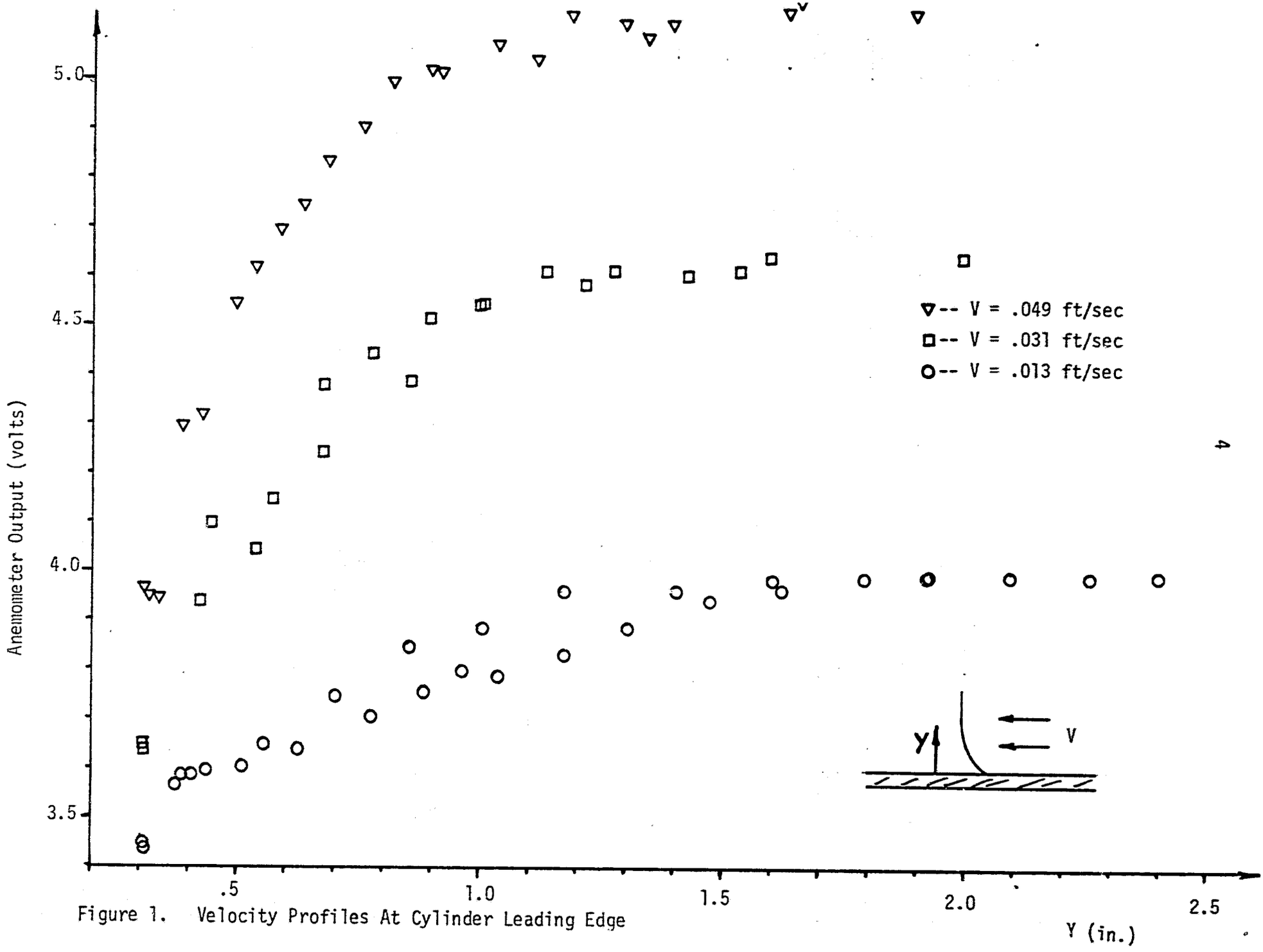

Figure 1. Velocity Profiles At Cylinder Leading Edge

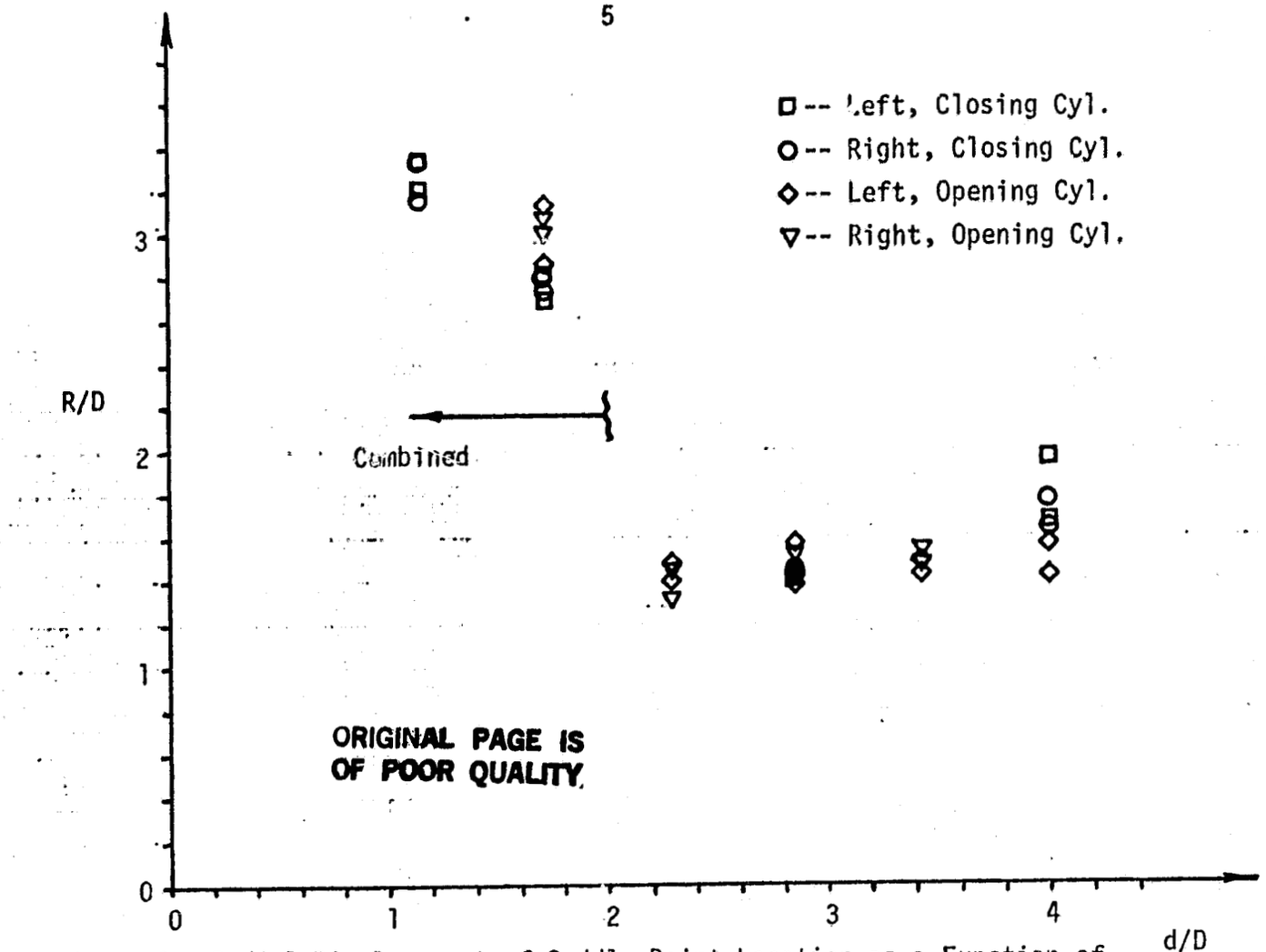

Figure 2a. Radial Displacement of Saddle Point Location as a Function of Cylinder Spacing

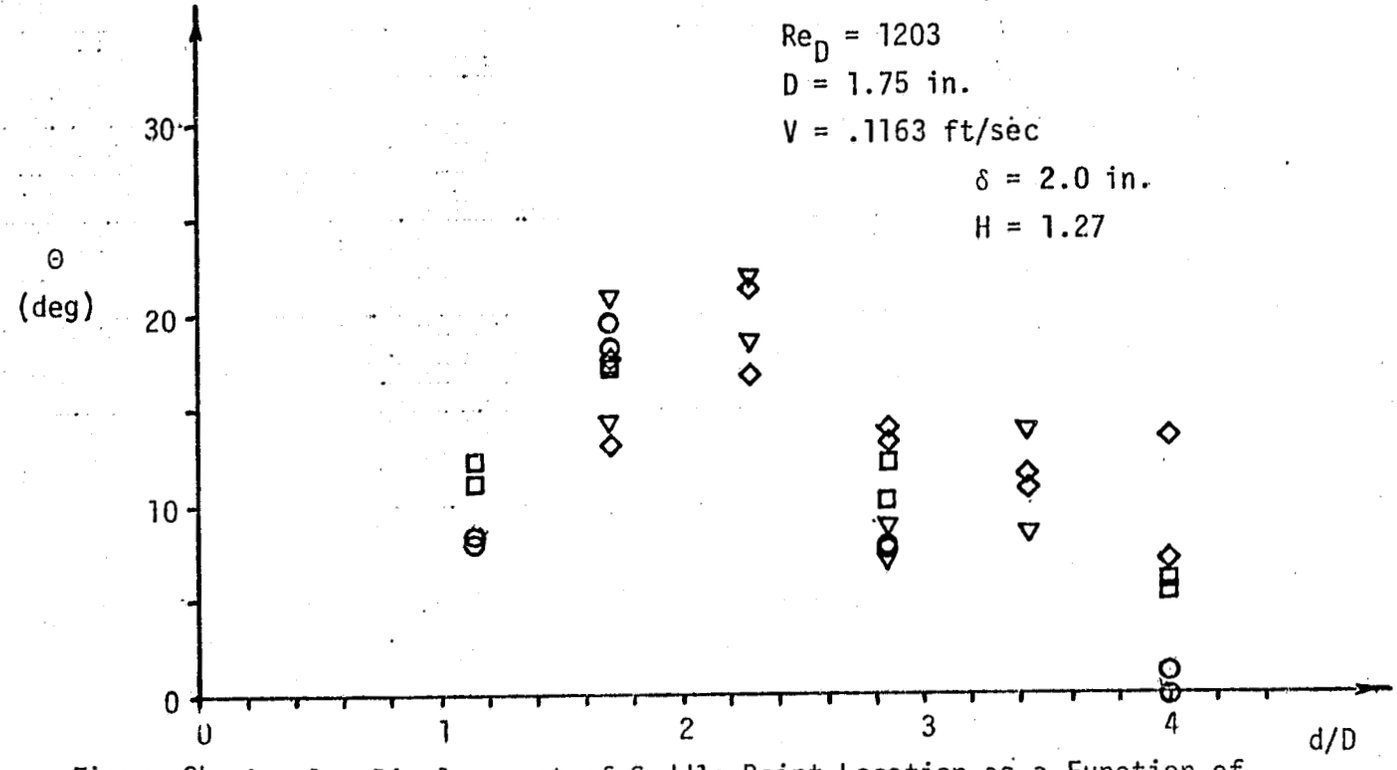

Figure 2b. Angular Displacement of Saddle Point Location as a Function of Cylinder Spacing

system on the floor. For some cases the limiting streamlines were "painted out" twice and pictures were taken of both to obtain a measure of accuracy and repeatability. Then after closing the cylinders they were opened up and data was taken that yields a measure of the repeatability of the position of the saddle points for a given cylinder separation.

Figure 2a shows the radial displacement of the saddle point location as a function of cylinder spacing. This is similar to the data presented in the first progress report[3] that was obtained using an open channel water table.

Figure 2b shows the angular displacement of the saddle point as a function of cylinder spacing. Again, the trend exhibited by this data is similar to the open channel data given in the first progress report.

There is considerable scatter in the data shown in Figure 2, and as such, it should be treated as preliminary. This scatter is due to a number of factors:

1) At lower Reynolds numbers (such as is the case in Figure 2), the vortex structure was found to be complex and oscillatory. As many as four or five vortices could be observed in the flow immediately upstream of each cylinder. Similar flow phenomena have recently been reported on by Baker[4] for low-speed air flow around a single cylinder.
2) Later testing showed that air could be trapped in the honeycomb and screens, leading to a flow distortion in the test section. This may have contributed to the scatter shown in Figure 2.

Consequently, in order to run at higher Reynolds numbers and eliminate trapped air, a new inlet section has been constructed, so that before each

run the honeycomb and screens can be put in place under water so that there is no trapped air bubbles. Tests using this new inlet section will be conducted during the next reporting period.

Wind Tunnel Construction and Assembly

During the reporting period the construction and assembly of the wind tunnel was completed. An overall view of the tunnel is shown in Figure 3.

Reference kiel and pitot probes were mounted upstream of the test section and were connected to a multitube water manometer, along with the static taps on the inlet. The blower motor was wired into the laboratory electrical system and the tunnel was first run on February 12, 1980.

As was noted in the last progress report, the Flexcore honeycomb for the inlet was a long lead-time item, and was not received until April 1980. The initial checkout of the tunnel (without the Flexcore) showed that at a blower vortex valve setting of about 70°-80° (90° is wide open) the test section velocity was 100 ft/sec, just about on design. Thus, testing will be possible at Reynolds numbers that are realistic, as was planned.

After the Flexcore was received it was "sewn" onto the outside of the porous plate of the inlet with thin transformer wire. Holes were drilled in the top endwall of the tunnel at the middle of the test section and at the exit of the inlet, every 6" across the 6 foot span of the tunnel. A probe actuator could be mounted at each one of the holes so that a pressure and velocity profile could be made, endwall to endwall. In addition, a set of stairs and a platform was constructed on top of the test section to provide ready access to the probe actuator.

Since the tunnel has been in operation, it has been found that the blower vibrates the test section to some degree. A rubber diaphragm had

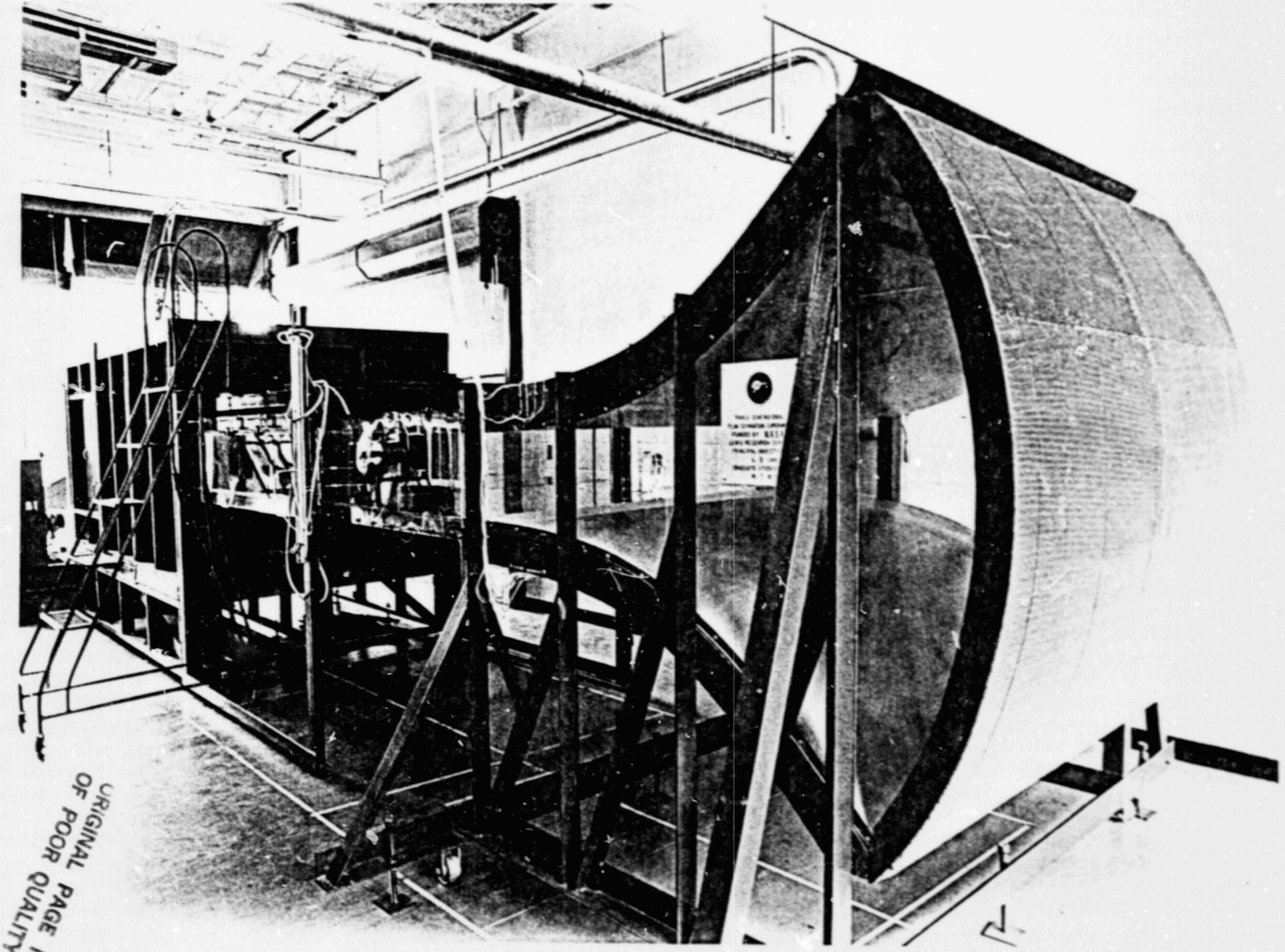

Figure 3. Overall view of wind tunnel showing honeycomb mounted on porous plate at inlet, Stanitz inlet nozzle, straight duct, test section with ladder, dump diffuser and blower.

been used to connect the blower to the diffuser, but this has not proven to be up to the task of eliminating all vibration. Some vibration is also transmitted through the floor.

In the last few weeks, steps have been taken to eliminate the blower vibration by mounting the blower on springs and installing a flexible duct between the blower and the diffuser. To a first approximation the transmissibility, T, of the spring-blower-mass system is given by

$$T = \frac{1}{\left(\frac{\omega_f}{\omega_B}\right)^2 - 1} \tag{1}$$

where damping has been neglected and where

- T = transmissibility, i.e. the force due to the blower vibration transmitted through the springs to the floor, divided by the same force for a rigid mounting.
- ω_f - the frequency of the blower vibration (roughly 1800 rpm).
- ω_B - the natural undamped frequency of the blower mass-spring mount system.

The last term, ω_B is given by

$$\omega_n = \sqrt{\frac{K}{m_B}} \tag{2}$$

where

- K - spring constant
- m_B - blower mass

It can be seen from (1) and (2) that to minimize T, the mass of the blower, m_B, should be large. One can do the same thing with a smaller value of

K, but there is a practical lower limit on K. [If the springs are too soft (low K) the blower will have a tendency to "jump" around]. Thus, to lower T, about 3000 pounds of concrete were poured into the base of the blower. When this cures (about mid-July 1980), the spring mounts and the flexible duct will be installed, and the concrete base and blower will be raised off the floor.

Wind Tunnel Testing

During the reporting period an extensive test program was undertaken to check out the characteristics of the wind tunnel, before any model testing was done.

First the static pressure distribution of the Stanitz inlet was measured, using the wall pressure taps that had been installed for that purpose. All pressures were measured relative to the static pressure of the pitot static reference probe upstream of the test section. The pressure differences were read using a Flow Corporation micromanometer that is accurate to $\pm$ 0.0002 in. of manometer fluid (N-butyl alcohol).

Figure 4 shows the pressure distribution that was measured along the centerline of the inlet, as a plot of q/q_∞ (local velocity head, $\frac{1}{2}\rho V^2$, over reference velocity head, $\frac{1}{2}\rho V_\infty^2$) vs. surface distance along the inlet. The reference velocity was calculated from the reference total pressure measured in the inviscid portion of the flow upstream of the test section and the static pressure measured at the point x = 0.5 ft. at the lower surface of the inlet. This value was used rather than the velocity measured at the test section because the latter is slightly higher due to the displacement thickness effects of the tunnel boundary layers.

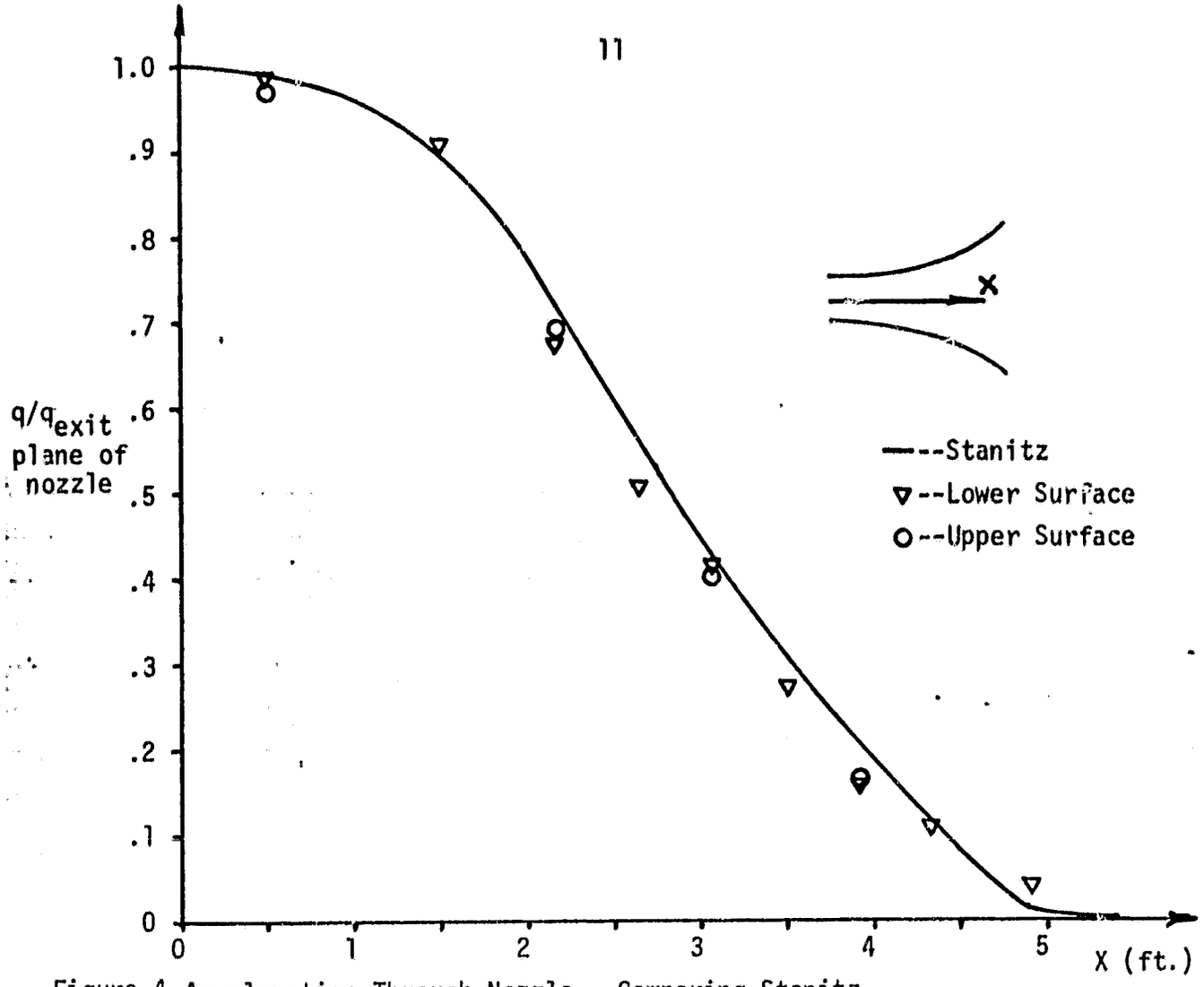

Figure 4. Acceleration Through Nozzle - Comparing Stanitz To Static Pressure Taps

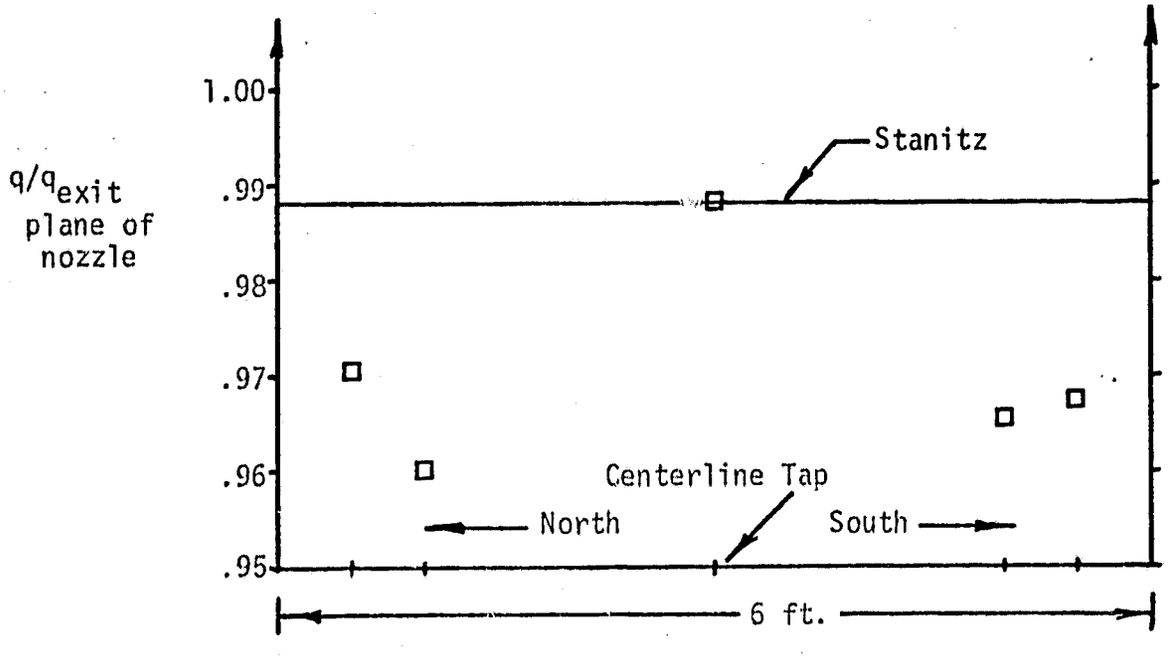

Figure 5. Nozzle Cross-Section -- 6 in. Upstream of Nozzle Exit Plane

Also plotted in Figure 4 is the Stanitz potential flow pressure distribution that the inlet was designed from. As can be seen, there is good agreement with potential flow on the nozzle inlet centerline for both the top and bottom of the inlet.

Figure 5 shows the static pressure distribution across the exit of the nozzle inlet on the bottom surface. The measured values of static pressure show some variation (note that ordinate scale has been expanded) away from the tunnel centerline. While this variation is not large, its presence is disturbing, since the inlet was carefully designed and constructed to provide uniform flow. More will be said about this variation in what follows.

Total pressure profiles were measured midway through the test section and upstream, at the exit of the inlet, using a United Sensor $\frac{1}{8}$" head kiel probe, with an acceptance angle range of $\pm 45°$. All pressure differences were measured with the micromanometer described above. The probe was positioned using an L. C. Smith probe actuactor, Model No. BBR-123-360. The actuator had been calibrated for position and yaw angle before the tests. Using the 3½ digit digital panel meter on the probe actuator indicator, the probe position could be read to $\pm$ 0.02" and the probe yaw angle to within $\pm$ 0.4°.

The test section has a 1x6 ft. cross-section. At the test section, traverses of total pressure were taken from floor-to-ceiling (the 1 ft. dimension) at locations 6 in. apart from the north side to the south side of the tunnel (the 6 ft. dimension).

Three of these total pressure traverses are shown in Figure 6, where distance from the tunnel floor is plotted against the total pressure coefficient, Cp_t, given by

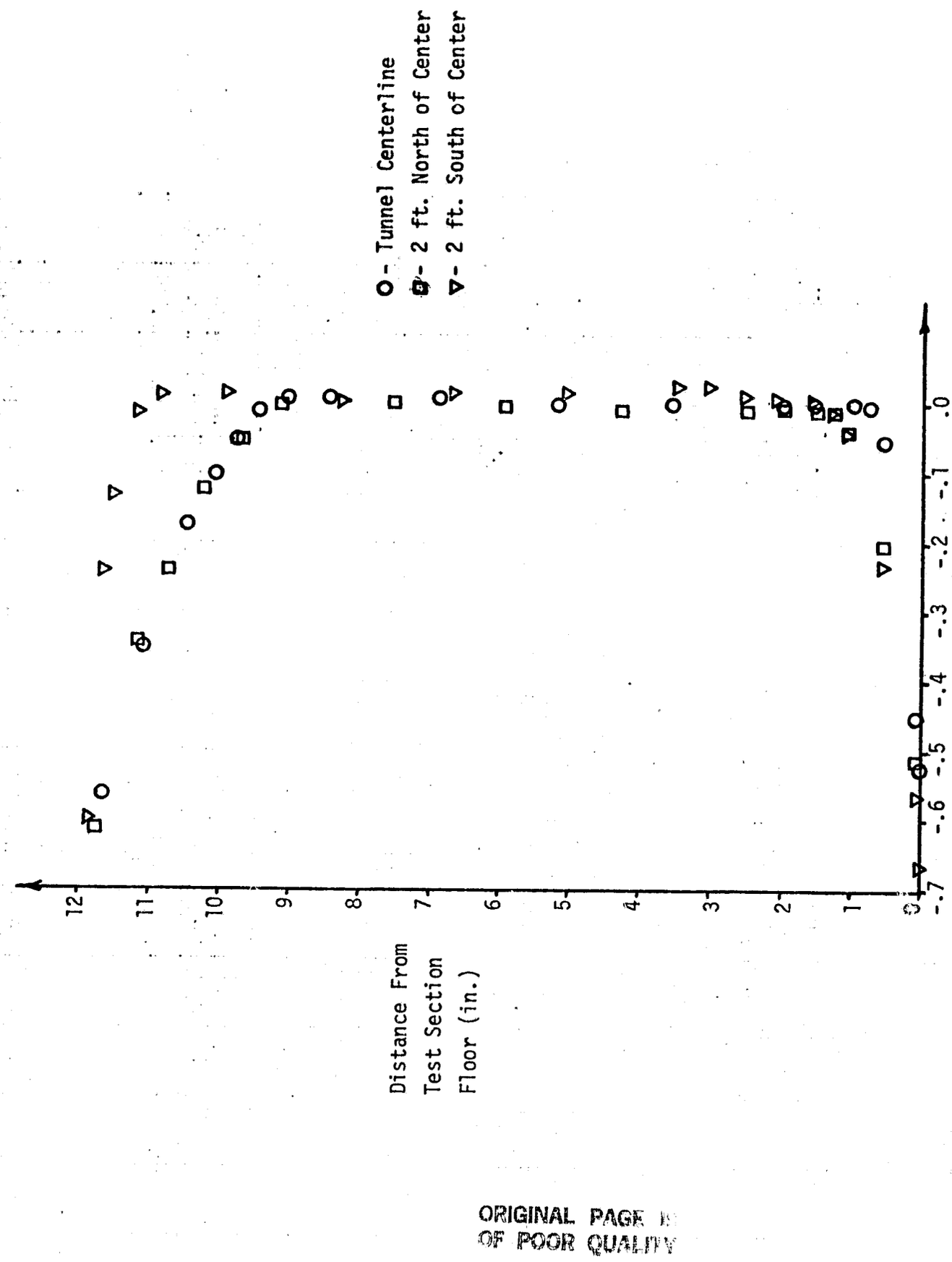

Figure 6. Total pressure profiles at the test section.

$$C_{P_t} = \frac{P_T - P_{T_\infty}}{\frac{1}{2}\rho V_\infty^2}$$

where P_T - measured total pressure

P_{T_∞} - reference total pressure (always measured with reference probe on north side of tunnel).

The data in Figure 6 shows that the inviscid core of the flow in the test section is fairly uniform in total pressure except at the south side of the tunnel, where the total pressure is slightly higher (about 1-3% which amounts to approximately 0.01-0.03 in. of water) than the centerline and north side total pressures. Secondly, the tunnel floor boundary layer gets thicker from the centerline to either the north or south, while the ceiling boundary layer is thinnest on the north wall. Thirdly, the data in Figure 3 shows that the ceiling boundary layer is larger than the floor boundary layer.

The slightly non-uniform static pressure distribution at the inlet exit, the slightly non-uniform total pressure distribution at the test section and the asymmetric boundary layers on the test section floor and ceiling are not to be expected, considering the care that was taken in the design and construction of the inlet.

The internal surfaces of the tunnel were inspected and it was found that the tunnel ceiling had one joint that caused a small front facing step. This was corrected but no change in the flow field was noted.

In an attempt to make the floor and ceiling boundary layers more alike, a trip wire was installed at the exit of the inlet. The wire was D = 0.02 inches in diameter and was chosen based on a trip Reynolds number of

$$\frac{U_\infty D}{\nu} \approx 900$$

based on the criteria given in Schlichting[5]. Total pressure measures were again taken at the test section and showed that the trip wire had little or no effect on either the ceiling or the floor boundary layers. Another test was done using a larger trip wire (D = 0.125") which also showed no effect on the test section boundary layers.

Traverse holes were then cut at the exit of the inlet, and traverses were taken every 6 inches (in the 6 foot dimension) with both the keil probe and a United Sensor pitot probe. Data from three of these traverses is shown in Figure 7. Figure 7a shows velocity and Figure 7b shows total pressure. The velocity plot shows that there is a slightly higher velocity in the south side of the tunnel. The total pressure traverses show essentially the same features as test section traverses, but scaled down, since the inlet traverses are about 6 feet upstream of the test section traverses.

Thus far, the conclusion is that the flow distortion and boundary layer asymmetry is coming from the inlet. Efforts are now under way to see if these effects are (a) being generated by the inlet itself (porous plate honeycomb, etc.), or (b) entering the inlet from the room itself and are not being sufficiently smoothed out by the porous plate.

Model Design and Construction

During the reporting period the first pair of cylinder models for the wind tunnel were designed. Construction of these models is now in the final stages. A photograph of one of the cylinder models is shown in Figure 8. The model is an aluminum cylinder that was accurately machined on a lathe to an outer diameter of 6.25 inches.

The two cylinders will be placed side-by-side in the wind tunnel test section by inserting each of them through an airtight fixture in the top

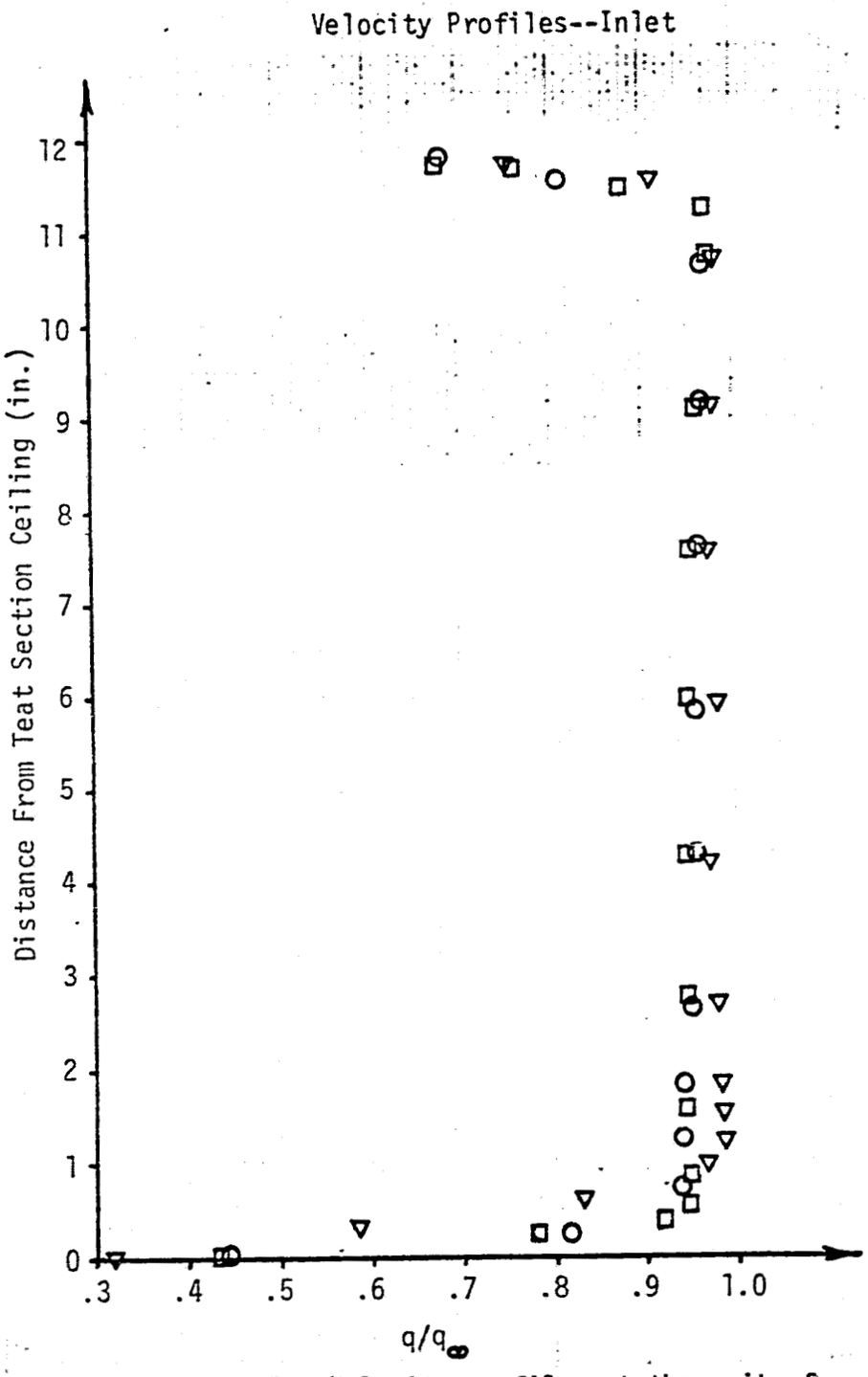

Figure 7a. Velocity profiles at the exit of the inlet.

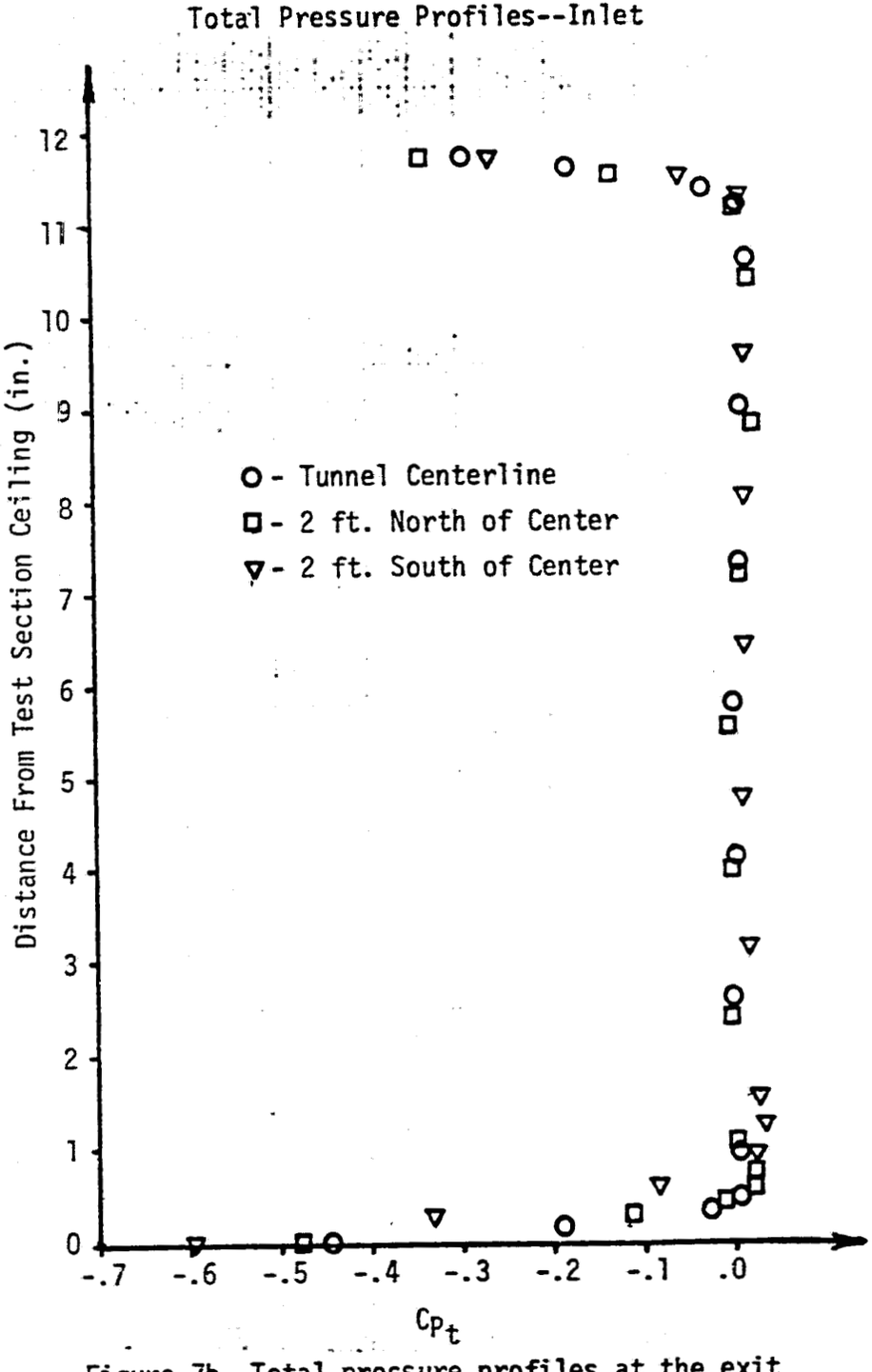

Figure 7b. Total pressure profiles at the exit of the inlet.

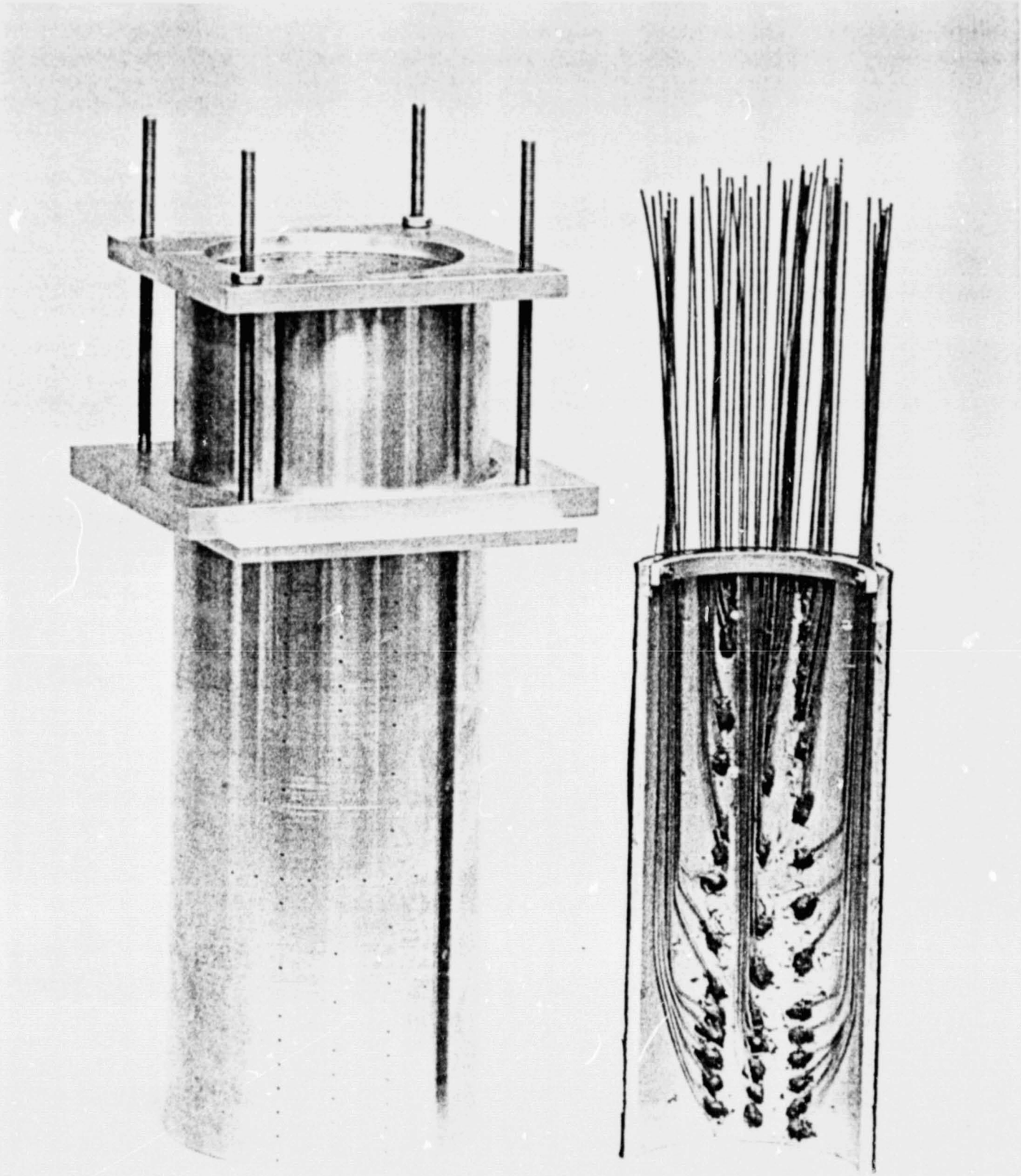

Figure 8. Wind tunnel cylinder model. At left is 6.25" OD aluminum cylinder with 59 static pressure taps, and mounting fixture. At right is pressure tap manifold.

of the test section. A clamping device (see Figure 8) will hold them in place and will press each cylinder against the floor of the test section. An O-ring at each cylinder base will seal the cylinder - test section floor junction.

Each cylinder has 59 pressure taps, with the greatest number of taps near the base of each cylinder, where the separation process will occur. The cylinders and the clamping fixture are constructed in such a way that a cylinder can be rotated (indexed) to change the relative circumferential location of the 59 pressure taps.

The pressure taps are connected on the inside of the cylinder to a manifold of 0.047" ID stainless steel capillary tubes. The use of this manifold (shown in Figure 8) allows the model to be constructed from a single, more sturdy, cylinder, rather than cutting the cylinder in half and individually soldering each capillary tube to each pressure tap.

The spacing between the cylinders can be varied by use of various size plexiglass spacers in the top of the test section. Since the bottom of each cylinder has a compressed O-ring seal, the floor of the test section can be kept clean (no junctions or seams) for the flow visualization experiments.

The construction of these first cylinder models should be completed by mid-July 1980, at which time flow visualization and pressure measurements will be done for a range of cylinder spacings.

Analytical Work

A two-dimensional potential flow program obtained from Professor Patrick Kavanaugh of Iowa State University was adapted to the UConn Computer System.

This program is based on the distributed source-sink method of Smith and Pierce. It is an on-body program, i.e. as output, it provides pressure distributions on the body itself. The output of this program will be used to compare with the experimental data from the pressure taps on the cylinders, to show any departure from potential flow.

Off-body pressure will also be taken and it is necessary to compare this data with a potential flow calculation. Thus during the reporting period, an off-body two-dimensional potential flow program for flow around two cylinders was completed. A discussion of this program is given in Appendix B. This program will be used to:

a) provide an early first-order correlation of saddlepoint location (gotten from flow visualization data) and potential flow pressure gradients at the saddlepoint location.

b) compare to flow field experimental data.

A third computer program has also been worked on and adapted to the UConn Computer System. This program was also obtained from Professor Kavanaugh, and is a general, two-dimensional contour plotting routine to be used in conjunction with a Calcomp Plotter. This program gives us the ability to plot isobars, streamlines, etc., be it from experimental data or from the output of a potential flow program.

Overview of Program

As noted in the last report[1] the water tunnel tests are behind schedule due to the inlet distortion problems that were encountered. However, the tests are far enough along to give us a good feel for cylinder spacing, wall effects, and low Reynolds number behavior, all of which have impacted wind tunnel model design.

The wind tunnel testing is slightly behind in schedule. The cylinder models will shortly be ready to be installed in the wind tunnel to check them out, but no data will be taken until the wind tunnel flow has been made more uniform.

Once better uniformity is achieved, testing will begin. The first tests will be to vary cylinder spacing and get the location of the saddle points by using flow visualization techniques.

The off-body potential flow program will be used to calculate normal and streamwise pressure gradients at the saddlepoint locations. This will give a first order correlation. Detailed flow measurements will then follow.

Acknowledgements

The work reported here has been carried out by Mr. Michael T. Boyle, a graduate student in the Mechanical Engineering Department and by the principal investigator. Mr. Russell Arnold and Mr. Scott Jamieson provided technical help. Mr. Craig Wagner, a Mechanical Engineering senior, completed the off-body potential flow program. Mr. Keith Simmons, also a Mechanical Engineering senior, completed the design, construction and check-out of the hydrogen bubble generator.

References

1. Langston, Lee S., "Turbine Endwall Two-Cylinder Program", Semi-Annual Status Report, July 1, 1979 - January 1, 1980.

2. Bradshaw, P., Experimental Fluid Mechanics, 2nd ed., Pergamon Press, 1970, pp. 80-81.

3. Langston, Lee S., "Turbine Endwall Two-Cylinder Program", Semi-Annual Status Report, January 1, 1979 - July 1, 1979.

4. Baker, C. J., "The Laminar Horseshoe Vortex", J. of Fluid Mech., 1979, 95, pp. 347-367.

5. Schlichting, H., Boundary-Layer Theory, 7th ed., McGraw-Hill, 1979, pp. 536-539.

APPENDIX A

The Hydrogen Bubble Generator

Introduction

The purpose of this project was to produce a hydrogen bubble generator for use as a flow visualization medium in a flow of water. Herein we present an explanation of the chemical processes involved in bubble generation as well as the design of a simple device for that purpose.

Background

In many fluid mechanics investigations there is a great need for visualization of complex fluid patterns. Flow visualization provides a means for exploring some flow phenomena that are not predictable by mathematical theory. Using hydrogen bubbles as tracer particles in a water flow is a good visualization technique. The first to apply this technique was a German scientist named F. X. Wortmann[1] who was followed in the United States by E. W. Geller[2,4]. Clutter and Smith[3] of Douglas Aircraft Company completed extensive research perfecting the hydrogen bubble visualization technique.

Theory

The hydrogen bubbles are produced by the electrolysis of water and must be of a size and quantity so as not to disturb the flow field. The electrolysis of water is a simple reaction which decomposes water into its basic elements:

$$H_2O \longrightarrow H_2 + \tfrac{1}{2}O_2$$

This reaction does not occur spontaneously therefore energy must be supplied.

As seen in the chemical equation above, there are twice as many moles of hydrogen produced than there are moles of oxygen. By applying Avogadro's Law at constant temperature and pressure it can be seen that, volumetrically, there are twice as many hydrogen bubbles produced as there are oxygen bubbles. It is for this reason that we choose to use hydrogen bubbles rather than oxygen bubbles to trace the flow.

The reaction occurs as follows: for the simple electrolysis cell shown in Figure A-1, oxygen bubbles are produced at the positive terminal, the anode, while hydrogen bubbles are produced at the negative terminal, the cathode.

The choice of a material (metal) to be used for terminals is based upon the chemical reactions that take place at the terminals as well as a strength requirement. (The H_2 source or cathode must withstand drag force of fluid). For instance, from the chemical reaction standpoint, platinum is a very good material.

The two reactions which take place at a platinum cathode (See Figure A-2) are:

$$2H^{+1}_{(L)} + 4e^{-1} + Pt^{+2}_{(S)} \xrightarrow{\Delta G_1} - PtH_{2(S)}$$

and

$$2H^{+1}_{(L)} + 2e^{-1} \xrightarrow{\Delta G_2} - H_{2(g)}$$

Note that the first reaction yields an undesirable solid precipitate, platinum hydrate, while the second yields the desired hydrogen gas. Both reactions require energy for them to proceed to the right. The energy required is called the free energy of formation (ΔG) and is much less for the gaseous hydrogen reaction than it is for the platinum hydrate reaction, i.e.,

$$\Delta G_2 \lll \Delta G_1$$

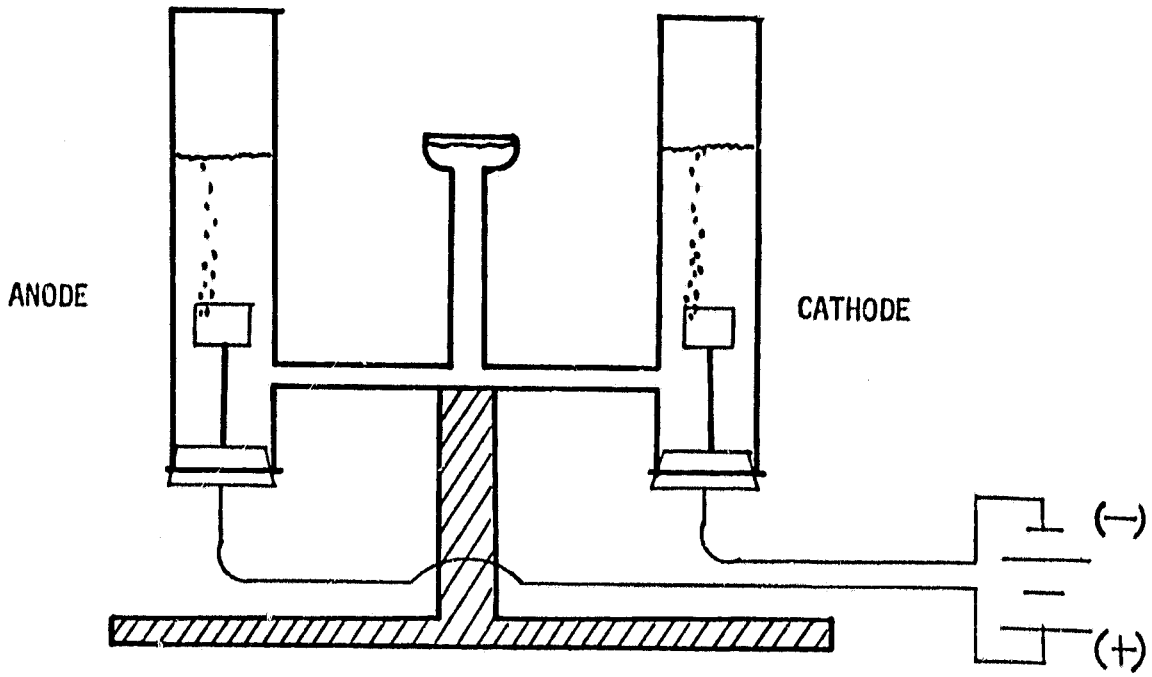

Figure A-1. An Electrolytic Cell

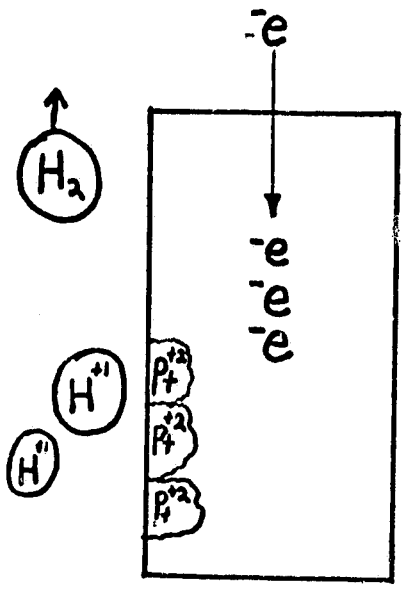

Figure A-2. Reaction at Platinum Cathode

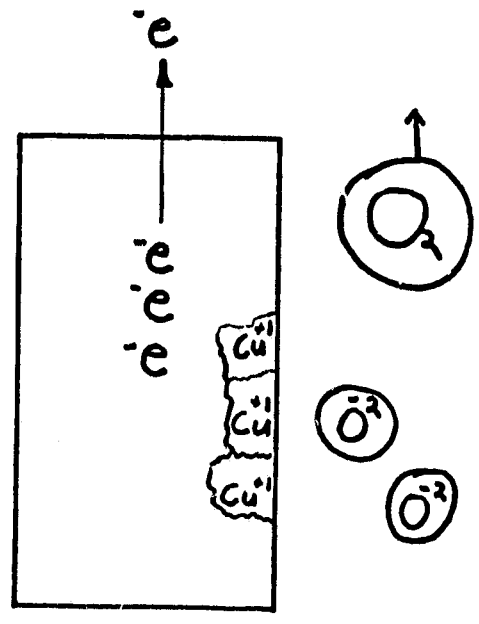

Figure A-3. Reaction at Copper Anode

Both reactions will occur but for all practical purposes no platinum hydrate will be formed. Platinum is also very corrosion resistive. However, in spite of all these advantages, platinum is limited in its use by its weakness. Other metals such as tungsten have been found to be an acceptable substitute. Tungsten has good corrosion resistance properties, along with good strength and a reasonable price.

At the anode we also have two chemical reactions. Again, platinum would make an ideal material for the terminal; however, a less expensive metal such as copper can be used (Figure A-3).

With a copper anode the two possible reactions are:

$$O^{-2}_{(L)} + Cu^{+1}_{(S)} \xrightarrow{\Delta G_3} Cu_2O_{(S)} + e^{-1}$$

and

$$2O^{-2}_{(L)} \xrightarrow{\Delta G_4} O_{2(g)} + 4e^{-1}$$

The free energy of formation of these reactions are close in value favoring the reaction which forms solid copper oxide. This will produce a large decay of the copper anode along with oxygen formation. This is not a great disadvantage in that we can probably install the anode in some unimportant region of the flow.

Application

Now that we have presented a methodology for hydrogen bubble formation we can discuss its application to flow in a water table.

The bubbles are introduced into the flow field by a carefully positioned, thin wire which will be designated as the cathode and energized accordingly. The anode terminal must then be placed anywhere in the water table in order to complete the cell. The anode is usually placed downstream of the test

section so as not to disturb the test section flow field (See Figure A-4).

In their research, Clutter and Smith[3] found that at flow velocities below 5 feet per second, wire diameters up to .005 inches could be used with little flow interference. Figures A-5, A-6, A-7, and A-8 are a graphic presentation of data taken by Clutter and Smith[3] and Mattingly[5] during their flow visualization studies.

To produce a continuous supply of bubbles, Clutter and Smith[3] found that a supply voltage of 25 to 400 volts is necessary, depending upon the resistance to current flow associated with the water table (electrolytic cell) being used. For our particular table, it was found that a voltage between 100 and 150 volts was sufficient to produce a continuous supply of bubbles adequate for good flow visualization. This voltage range yields a current range from .25 to .5 amps on our water table. The voltage and therefore current levels must be adjusted to give a "good" stream of bubbles (there must be enough bubbles so that they can be seen well, and they must not be so large that they float up) for each flow velocity tested. Currents can be increased for a given voltage level by seeding the water (table salt).

By pulsing the supply of voltage to the cell, a cyclic generation of hydrogen along the cathode wire produces patterns like those of Figure A-9. By measuring the pulse duration electronically a velocity profile can be obtained simply by measuring the pulse width. There are several pulse generators that can supply this signal, but not at the voltage and current required. To obtain the high voltage square wave (Figure A-10) a signal generator is used to activate an electronic switch to an additional power supply (Figure A-11). (A complete schematic is shown in Figure A-18.)

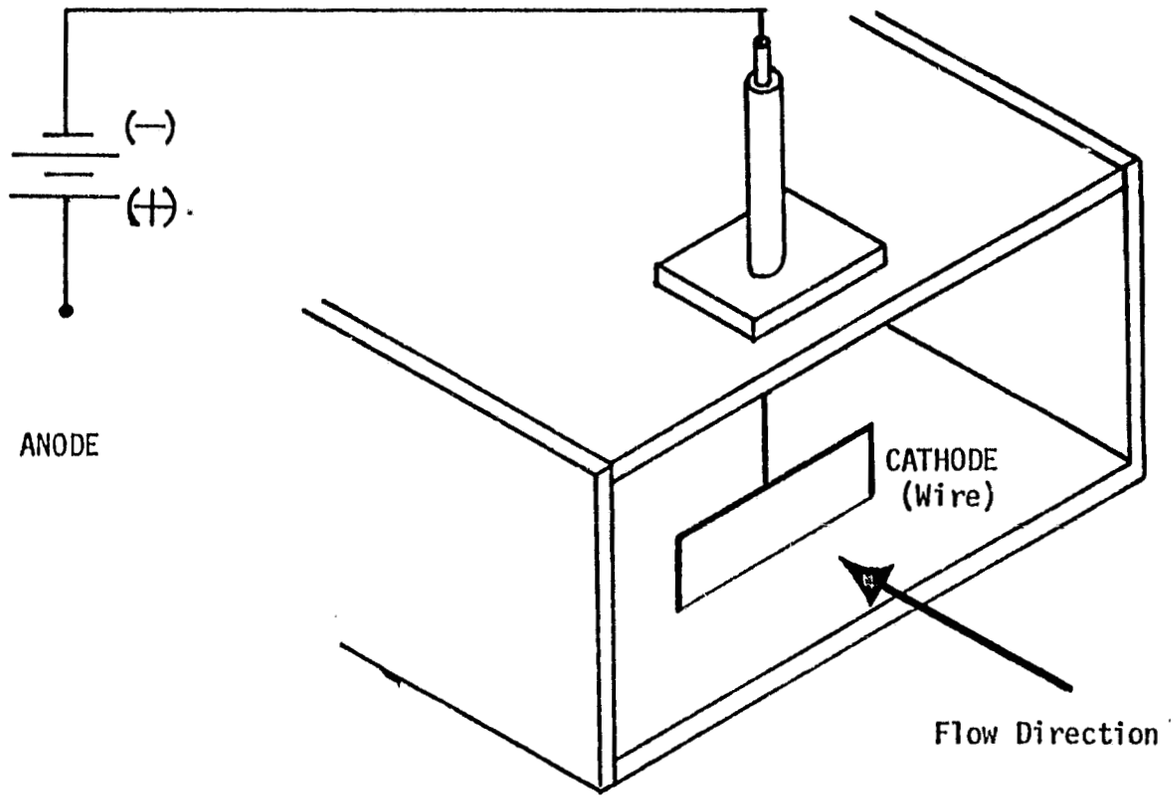

Figure A-4. Hydrogen Bubbles are Generated at the Wire Cathode

Figure A-5

$Re_D < 40$

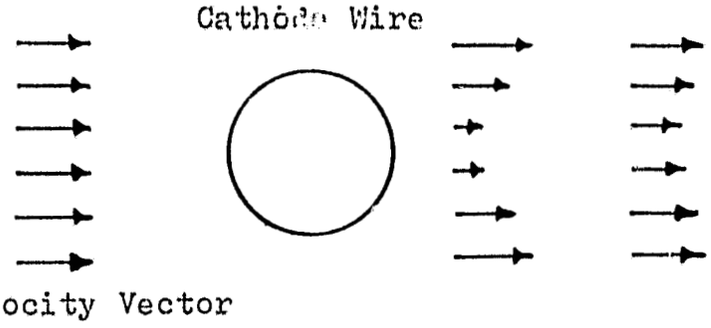

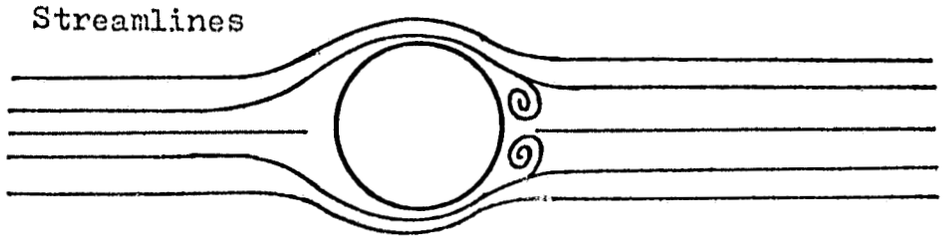

$Re_D < 40$

Figure A-6

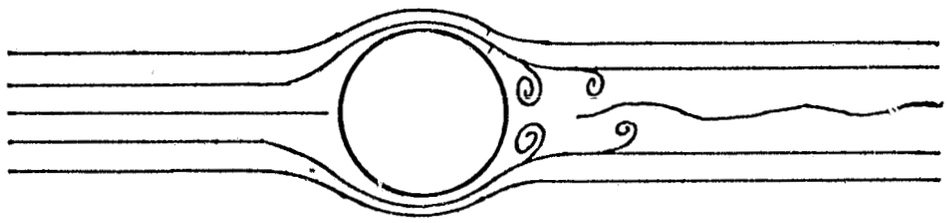

$40 < Re_D < 150$

Figure A-7

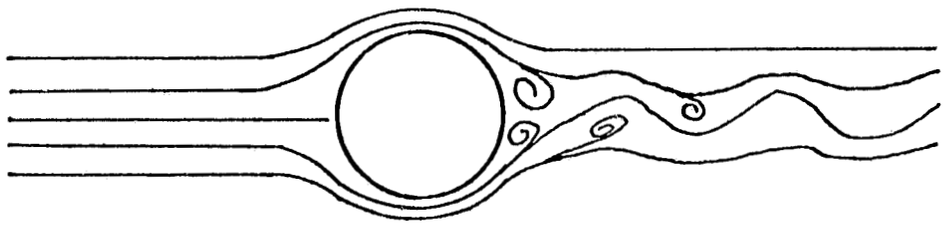

$150 < Re_D < 300$

Figure A-8

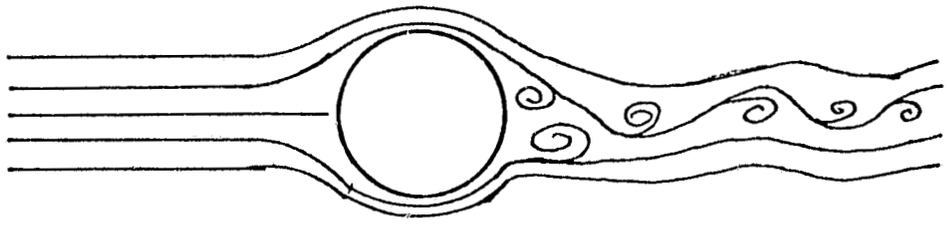

$Re_D > 300$

Flow Around a Cylinder for Various Reynolds Numbers, Re_D

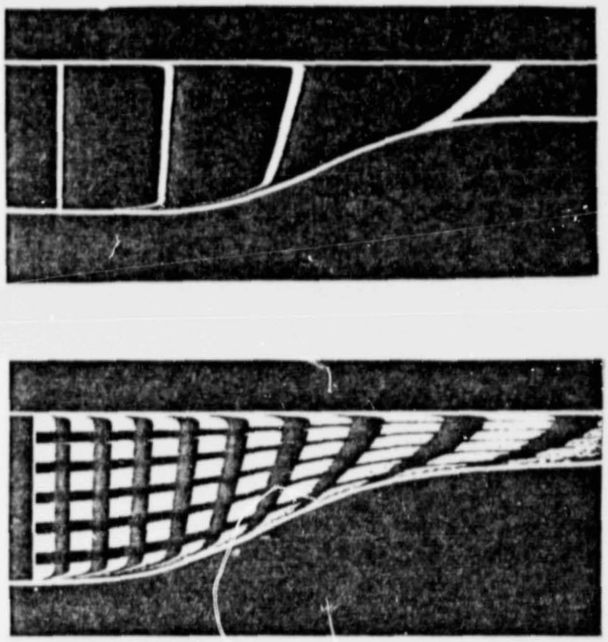

Figure A-9. Flow Through a Converging Channel, taken from Reference 7. Upper Photo shows Time Lines Made by Hydrogen Bubbles from Pulsed Wire. Lower Photo shows Combined Time-Streak Markers Produced by a Pulsed, Partially Insulated Wire.

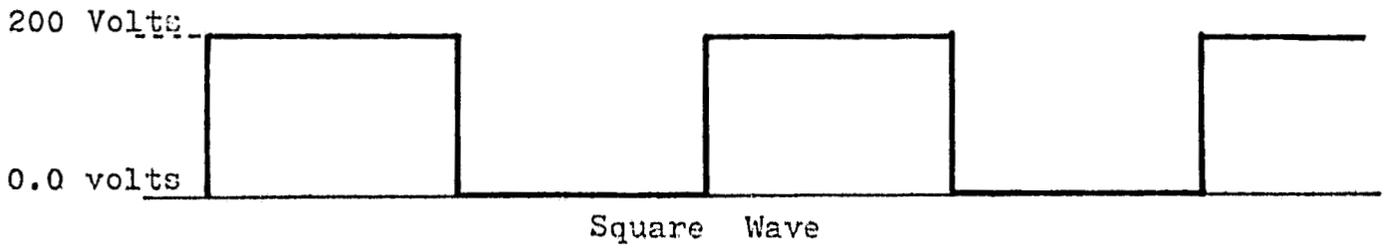

Figure A-10. A sharp, square wave of voltage is necessary to produce uniform bubbles.

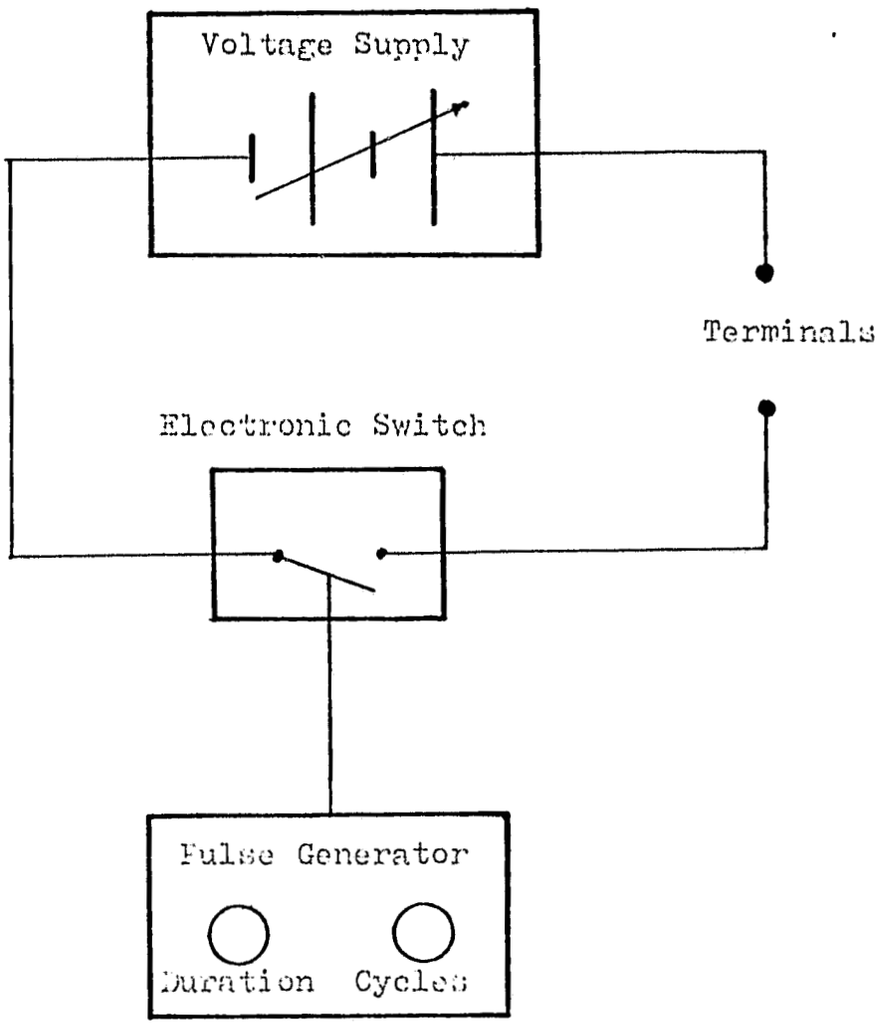

Figure A-11. Simplified electronic circuit of power supply.

It is necessary to have a sharp square wave of voltage in order to produce a consistent bubble size throughout the pulse width. Without the sharp square wave of voltage, the bubble size will vary throughout the pulse width causing large separation of the bubbles as the bubble sheet propagates through the test section (see Figure A-12). It can be seen in the figure that the slight variation in voltage causes inconsistent bubble sizes. The buoyancy and drag forces will be different for each bubble size causing the larger bubbles to move slower and rise more, while the small bubbles follow the flow stream.

Stoke's analysis of the forces on a buoyant sphere in a steady low-speed water flow, shows a buoyancy to drag ratio of:

$$B/D = \frac{gd^2}{18U\nu}$$

where d = bubble diameter

U = flow velocity

ν = kinematic viscosity

B = buoyancy force

D = drag force

It can be seen in Stoke's analysis that as the flow velocity decreases, or bubble diameter is increased, the buoyancy to drag ratio will increase, causing the bubbles to deviate from the flow field. A free body diagram on an individual bubble is given in Figure A-13. Bubble diameters between 0.0005 and 0.001 inches will have a rise rate due to buoyancy of about .05 inches per second. With a flow velocity between 0.1 and 5 feet per second this rise rate is insignificant.

Flow velocity and the diameter of the cathode wire play another role in determining bubble size. The faster the flow, the greater the drag forces

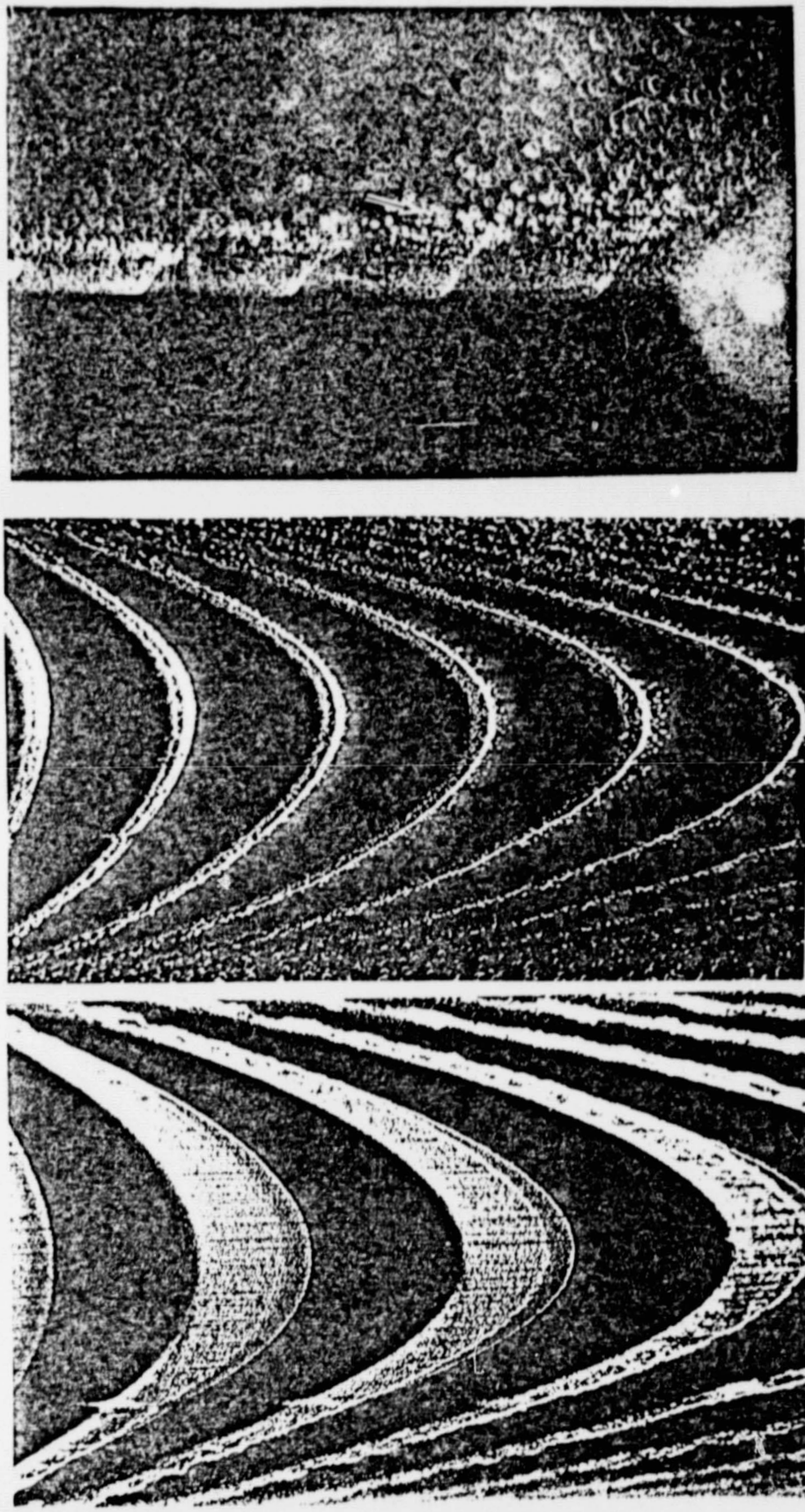

Figure A-12. At top, an edge view of pulsed time lines showing the effect of uneven bubble sizes. At middle and bottom, a top view of pulsed time lines showing a non-square wave behavior. Taken from Reference 8.

Figure A-13. To accurately follow the flow the buoyance to drag ratio must be small.

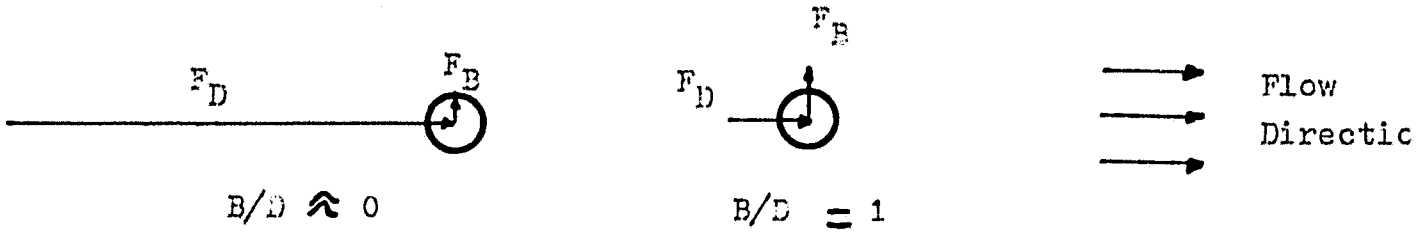

Figure A-14

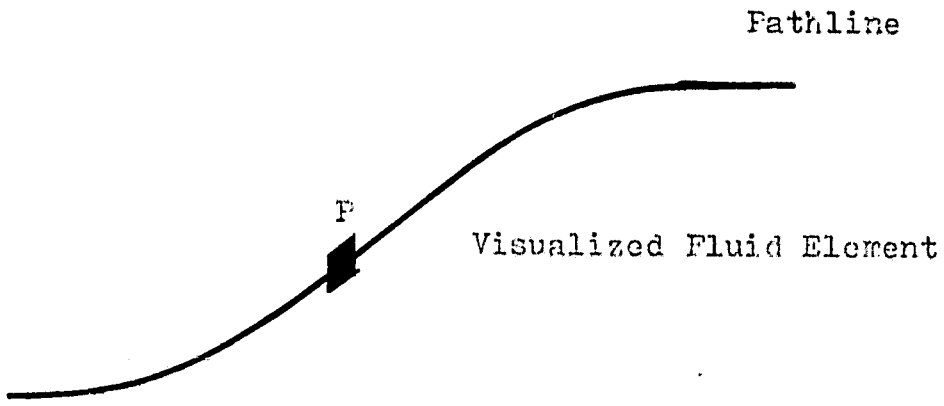

Figure A-15

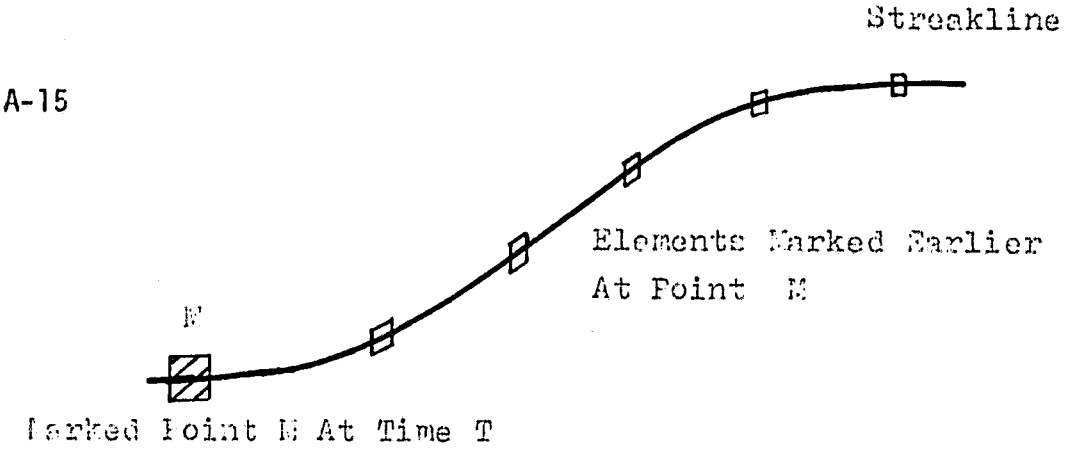

Figure A-16

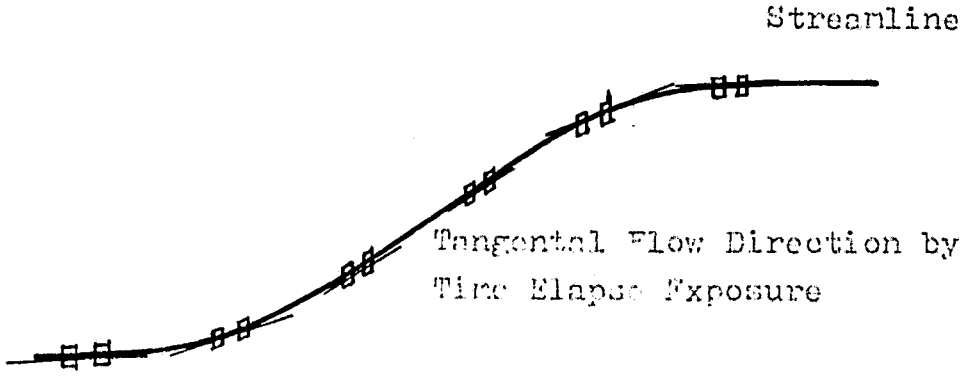

on the hydrogen gas around the cathode wire. This drag causes the gas to separate quickly from the wire thereby producing small bubbles.

Schraub and Kline[6], at Stanford University, perfected the techniques necessary to detect path lines, streaklines, and streamlines in low speed water flows (Figures A-14, A-15, and A-16).

Figure A-17 shows some possible configurations for lighting the stream of bubbles. It has been found that the 125° angle between the light source and the line of vision and the flat black color used for contrast, are important in getting good photos of the bubbles. Figure A-18 shows the circuit diagram of the electronics for the bubble generator, and Figure A-19 shows the bubble generator control panel.

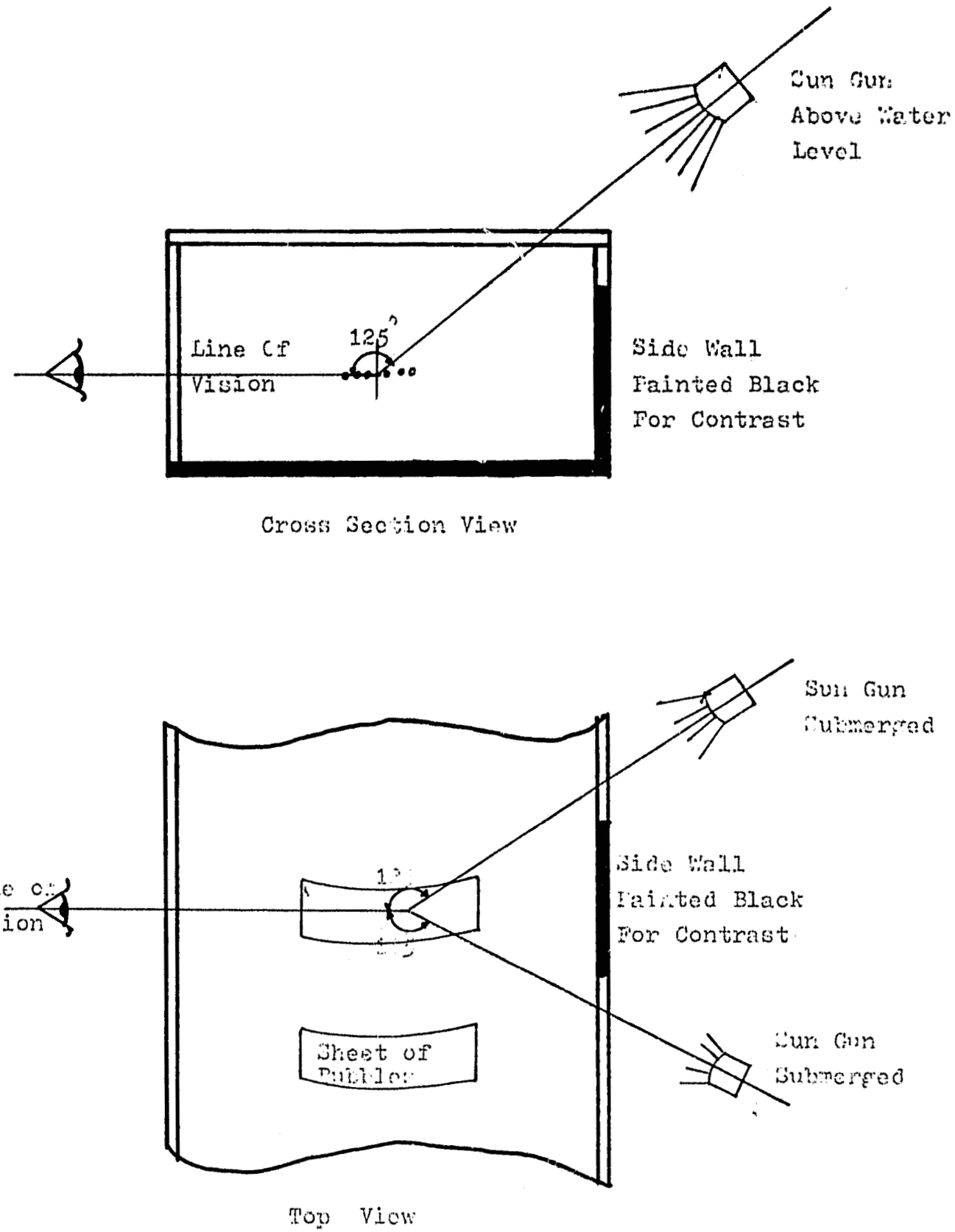

Figure A-17. Optimum lighti[illegible]igurations for viewing and photographing hydrogen bubb[illegible]

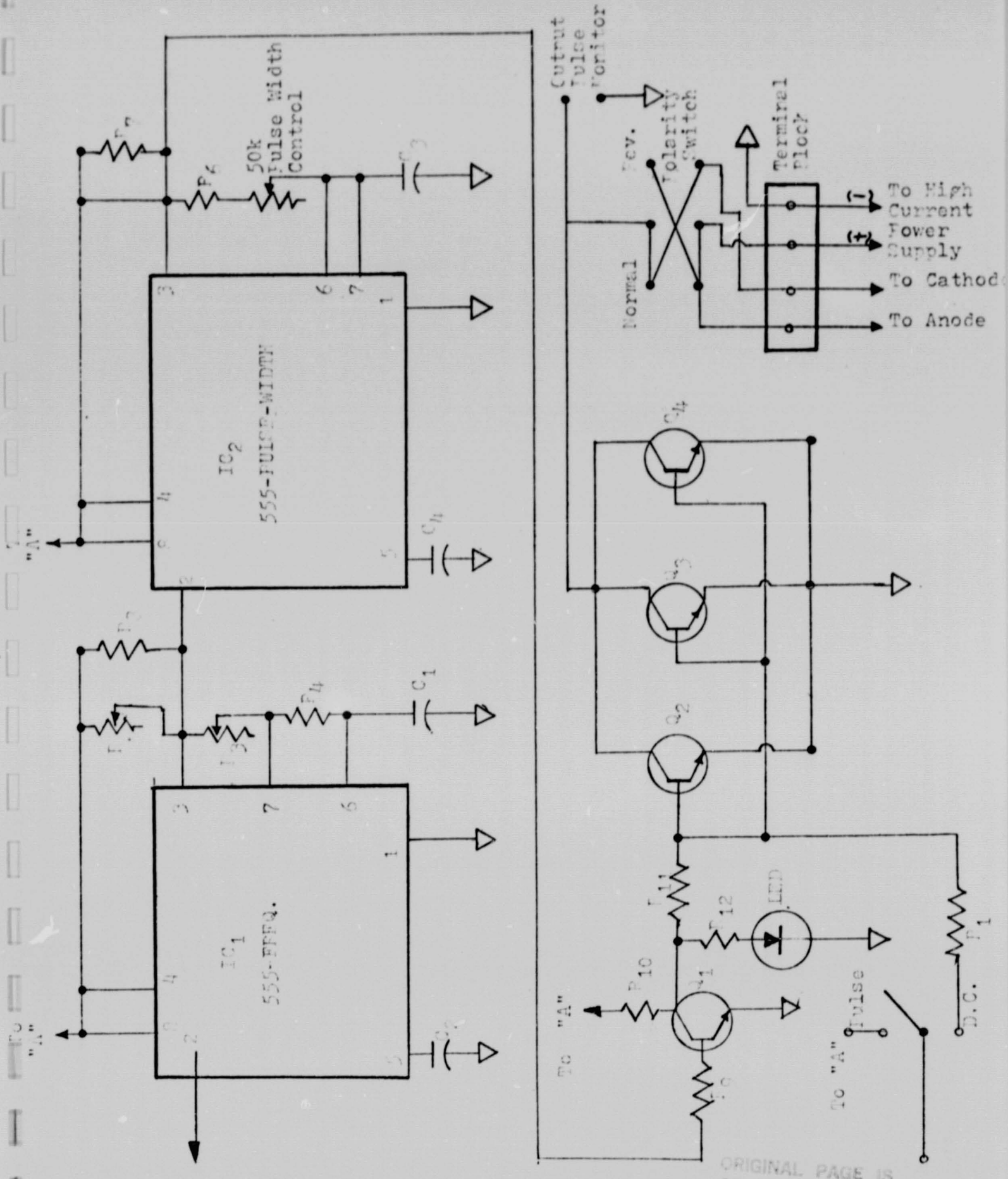

Figure A-18. Bubble Generator Schematic

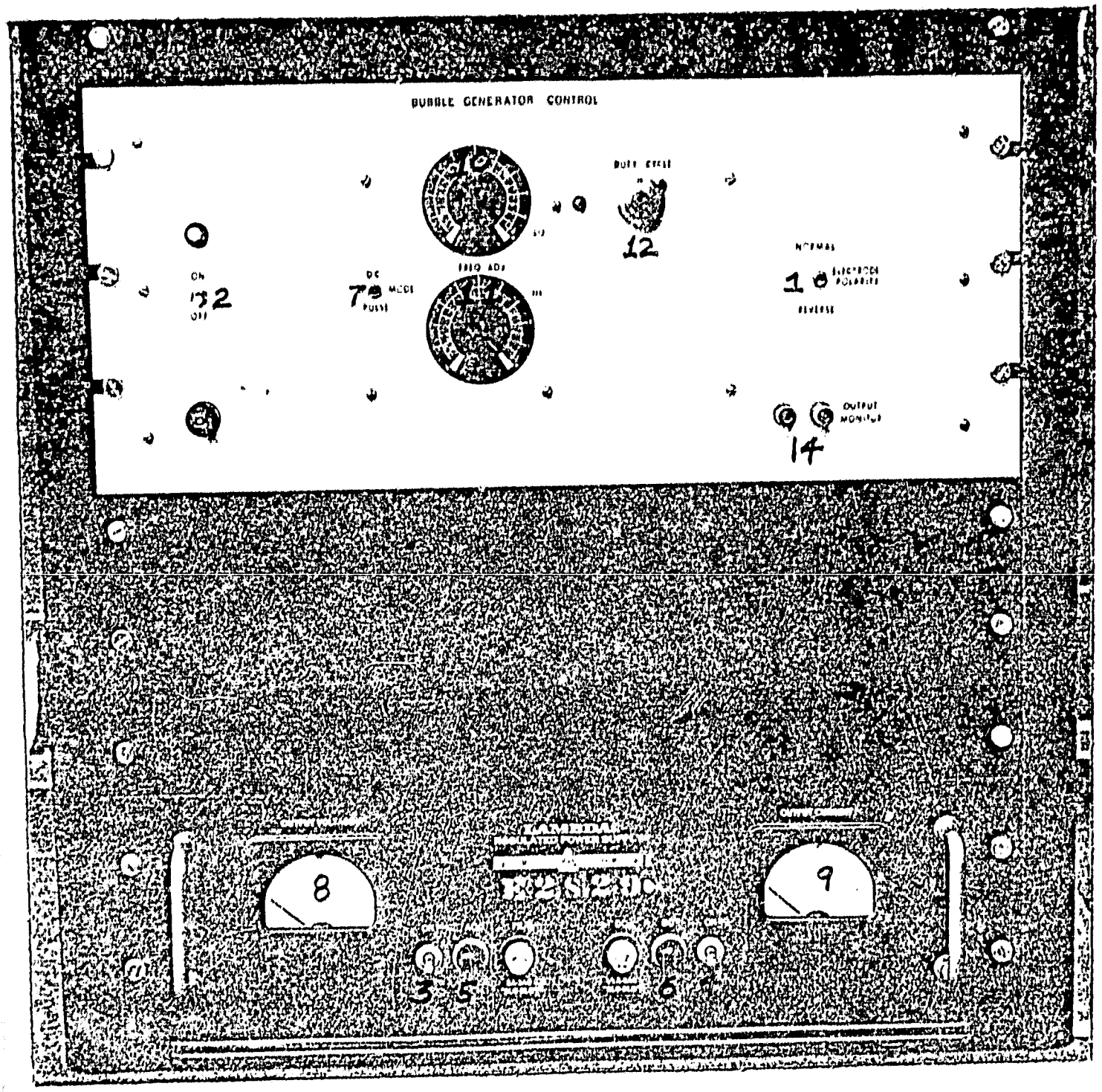

Figure A-19. Bubble Generator Control Unit and Power Supply.

REFERENCES

1. Wortmann, F. X., 1953 Z, Angew. Pys. 5, 201-6; 1962 Technical Translation, National Resourse Coun. Can. No. 1049.

2. Geller, E. W., Masters Thesis, Aeronautical Engineering Department, Mississippi State College, 1954.

3. Clutter, Darwin W., and Smith, A. D., "Flow Visualization by the Electrolysis of Water", Aerospace Engineering, Volume 20, 1961, p. 24.

4. Geller, E. W., 1954, Journal of the Aeronautic Science 22: 969-70.

5. Mattingly, George E., "The Hydrogen Bubble Flow Visualization Technique", David Taylor Model Basin, Navy, Report 2146, February 1966.

6. Schraub, F. A. and Kline, J. S., "Use of Hydrogen Bubbles for Quantitative Determination of Time Dependent Velocity in Low Speed Water Flows", Report MD-10, Stanford University, February 1964.

7. Kline, S. J., "Flow Visualization", National Committee for Fluid Mechanics Film, Stanford University.

8. Hearney, James J., "The Study of a Laminar Wake Produced by a Semi-infinite Plate in a Rectangular Channel", Ph.D. Thesis, University of Connecticut, 1970.

APPENDIX B

Two-Dimensional Off-Body Flow Program

Summary

The two-dimensional off-body potential flow program was developed to provide velocities, pressures, and streamlines in the flow field around arbitrary two-dimensional bodies. The bodies used in this program may be any series or arrangement of closed bodies, with lift and/or in an infinite cascade. The results are printed in a table for various points in the flow field. Options also exist for plotting isobars or streamlines on the Calcomp Plotter. Fundamental to the two-dimensional off-body potential flow program is the on-body potential flow program, as the parameters needed for the off-body program are generated by the on-body program. In addition to these two programs, a third program used in making plots of isobars and streamlines is a contour plotting program. This program and the on-body program are products of previous work at the University of Iowa.

Symbols

u	x velocity
v	y velocity
ψ	stream function
σ_i	source or sink of strength
U	unit free stream flow
Γ_K	strength of circulation
npts	total number of all body points
nobods	number of bodies in the flow field
s	length of line singularity
(x_p, y_p)	arbitrary point in the flow field
(x'_p, y'_p)	translated point in field
(x_m, y_m)	midpoint of line source segment
θ	angle of line source to horizontal
C_p	pressure coefficient
sp	cascade spacing
Re	real part of a complex function
Im	imaginary part of a complex function
z_1, z_2	complex vectors

Theory

The basis for potential flow calculations is the solution to Laplace's equation. Laplace's equation is derived through the irrotationality condition;

$$\frac{\partial u}{\partial y} - \frac{\partial v}{\partial x} = 0$$

In addition the stream function is defined as:

$$u = \frac{\partial \psi}{\partial y} \qquad v = -\frac{\partial \psi}{\partial x}$$

which gives after substitution into the irrotationality condition;

$$\frac{\partial}{\partial y}\left(\frac{\partial \psi}{\partial y}\right) - \frac{\partial}{\partial x}\left(-\frac{\partial \psi}{\partial x}\right) = 0$$

$$\frac{\partial^2 \psi}{\partial y^2} + \frac{\partial^2 \psi}{\partial x^2} = 0$$

This is Laplace's equation. A solution or set of solutions to Laplace's equation can be made into a sum which is also a solution. This condition of linearity facilitates the calculation technique used in this program.

Bodies in the flow field are represented by distinct points describing their contours. The program uses these points to generate line source-sink singularities which adjusts the free stream flow to that which satisfies the Neumann condition on the boundary of the bodies. In the case of lift the flow will satisfy the Kutta condition, also. The overall approach here is based on the work of Hess and Smith[1].

The stream function for a single source at the origin is given by:

$$\psi = \sigma_i \tan^{-1} y/x$$

Adding a free stream flow yields

$$\psi = Uy$$

and the contribution from circulation

$$\psi = -\frac{\Gamma}{2\pi} \log_e (x^2 + y^2)^{\frac{1}{2}}$$

gives the stream function for a single source located at the origin, with lift in uniform flow.

$$\psi = Uy + \sigma_i \tan^{-1} y/x \; - \frac{\Gamma}{2\pi} \; \ln(x^2 + y^2)^{\frac{1}{2}}$$

For every body point specified there is a corresponding strength of the source-sink singularity, σ_i. To account for all the body points a summation may be taken.

$$\psi = Uy + \sum_{i=1}^{npts} (\sigma_i \tan^{-1} y/x - \frac{\Gamma}{2\pi} \ln(x^2 + y^2)^{\frac{1}{2}})$$

Although the circulation value is similar for all points in the same body, if there is more than one body the circulation must be summed, yielding:

$$\psi = Uy + \sum_{i=1}^{npts} (\sigma_i \tan^{-1} y/x \; - \sum_{K=1}^{nobods} \frac{\Gamma_K}{2} \ln(x^2 + y^2)^{\frac{1}{2}})$$

The above value of the stream function is true for all different singularities, all located at the origin, however. Therefore each source-sink must take on the value of a line singularity, removed from the origin, and angled such that the sum total of all singularities maps out the bodies in the flow field. To develop the line singularities consider an element at the origin orientated as shown.

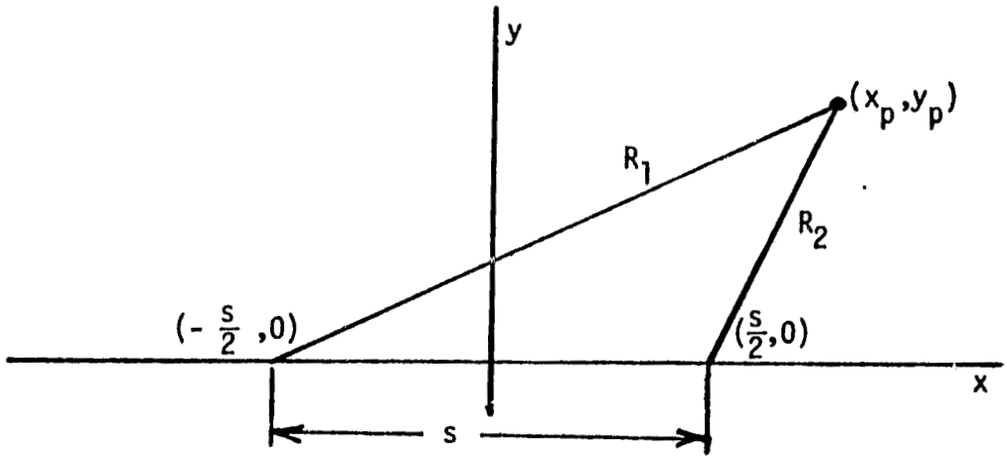

The stream function for the element can be found by integrating the source-sink function over the region -s/2 to s/2.

$$\psi = \int_{-s/2}^{s/2} \sigma_i \tan^{-} \frac{y_p}{x_p - x} \, dx$$

Making the substitution: $x' = x_p - x$, $dx' = -dx$, when $x = -s/2$, $x' = x_p + s/2$; and when $x = s/2$, $x' = x_p - s/2$. The stream function becomes:

$$\psi = - \int_{x_p+s/2}^{x_p-s/2} \sigma_i \tan^{-1} \frac{y_p}{x'} \, dx'$$

$$\psi = - \int_{x_p+s/2}^{x_p-s/2} [-\sigma_i \tan^{-1} \frac{x'}{y_p} + \sigma_i \pi/2] dx'$$

Since the value for σ_i is constant over each element, it may be taken outside the integral.

$$\psi = \sigma_i \int_{x_p-s/2}^{x_p+s/2} [\pi/2 - \tan^{-1} \frac{x'}{y_p}] \, dx'$$

$$\psi = \sigma_i [\pi/2 \, x' - \tan^{-1} \frac{x'}{y_p} \cdot x' + \frac{y_p}{2} \ln(1 + \frac{x'^2}{y_p^2})] \Big|_{x_p-s/2}^{x_p+s/2}$$

$$\psi = \sigma_i [\pi/2 \; s - (x_p+s/2)\tan^{-1}\frac{x_p+s/2}{y_p} + (x_p-s/2)\tan^{-1}\frac{x_p-s/2}{y_p} +$$

$$\frac{y_p}{2} \ln \frac{y_p^2 + (x_p+s/2)^2}{y_p^2 + (x_p-s/2)^2}]$$

A coordinate transformation must also be used, as each segment is not located at the origin with zero angle of orientation. The segment shown gives an example of how this transformation is accomplished. From the diagram it can be seen that subtracting x_m and y_m from the midpoint will bring the line segment center to the origin. A rotation, to the horizontal of the line segment may be accomplished by an angle, $-\theta$. The angle, θ, is found from geometry and is equal to

$$\theta = \tan^{-1}\frac{y_2 - y_m}{x_2 - x_m}$$

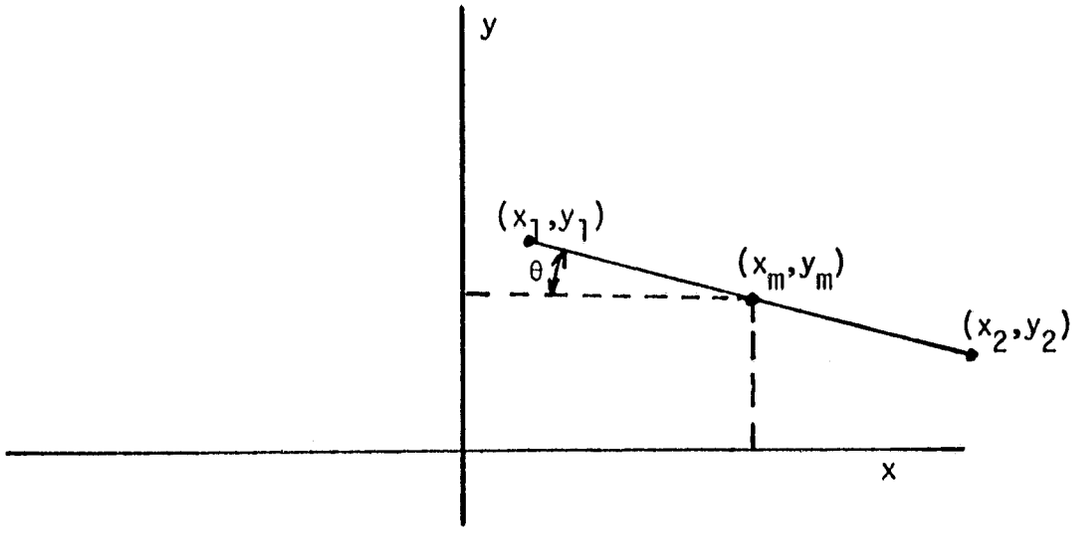

The correcting displacements to x_p and y_p are achieved by:

$$\Delta y = s/2 \sin\theta \qquad \Delta x = s/2 \cos\theta$$

The translation and rotation are applied to the point (x_p, y_p) and (x_p', y_p'); with:

$$x_p' = x_p - x_m - \Delta x$$

$$y_p' = y_p - y_m - \Delta y$$

Adding the effects due to free stream and circulation, the stream function now becomes

$$\psi = Uy_p + \sum_{i=1}^{npts} [\sigma_i(\pi/2\ s - (x_p'+s/2)\tan^{-1}\frac{x_p'+s/2}{y_p'} + (x_p'-s/2)\tan^{-1}\frac{x_p'-s/2}{y_p'} +$$

$$\frac{y_p}{2}\ln\frac{y_p'^2+(x_p'+s/2)^2}{y_p'^2+(x_p'-s/2)^2}) - \sum_{K=1}^{nobods}\frac{\Gamma_K}{2\pi}\ln(x_p'^2+y_p'^2)^{\frac{1}{2}}]$$

Now to calculate the velocities of the off-body points, apply the formulas

$$u = \frac{\partial\psi}{\partial y} \quad \text{and} \quad v = -\frac{\partial\psi}{\partial x}\ .$$

$$u = y_p + \sum_{i=1}^{npts}(\sigma_i\frac{1}{2}\ln\frac{(x_p'+s/2)^2+y_p'^2}{(x_p'-s/2)^2+y_p'^2} - \sum_{K=1}^{nobods}\frac{\Gamma_K}{2\pi}\ .$$

$$(\tan^{-1}\frac{x_p'+s/2}{y_p} - \tan^{-1}\frac{x_p'-s/2}{y_p}))$$

$$v = \sum_{i=1}^{npts}(\sigma_i[\tan^{-1}\frac{x_p'+s/2}{y_p'} - \tan^{-1}\frac{x_p'-s/2}{y_p'}] + \sum_{K=1}^{nobods}\frac{\Gamma_K}{2\pi}(\frac{1}{2}\ln\frac{(x_p'+s/2)^2+y_p'^2}{(x_p'-s/2)^2+y_p'^2}))$$

These are the formulas used in the calculation for velocity and pressure in the program. C_p, the pressure coefficient is calculated from

$$C_p = 1 - \frac{(u^2+v^2)^{\frac{1}{2}}}{U^2}$$

The velocities for a point in a cascade flow are calculated somewhat differently than the above formulas for uniform lifting flow. Calculations are arrived at in the complex plane. In the report for the on-body program, the author derives the velocity formulas using a complex potential function. For uniform flow and lift the formulas are given below, where sp equals the specified cascade spacing and α is the angle of the line source element with the horizontal.

$$u = U_{yp} + \sum_{i=1}^{npts} \left(\sigma_i \mathrm{Re}\left[e^{-i\alpha} \ln\left(\frac{\sinh \frac{\pi z_1}{sp}}{\sinh \frac{\pi z_2}{sp}}\right)\right] + \sum_{K=1}^{nobods} \frac{\Gamma_K}{2\pi} \mathrm{Im}\left[e^{-i\alpha} \ln\left(\frac{\sinh \frac{\pi z_1}{sp}}{\sinh \frac{\pi z_2}{sp}}\right)\right]\right)$$

$$v = \sum_{i=1}^{npts} \left(-\sigma_i \mathrm{Im}\left[e^{-i\alpha} \ln\left(\frac{\sinh \frac{\pi z_1}{sp}}{\sinh \frac{\pi z_2}{sp}}\right)\right] + \sum_{K=1}^{nobods} \frac{\Gamma_K}{2\pi} \mathrm{Re}\left[e^{-i\alpha} \ln\left(\frac{\sinh \frac{\pi z_1}{sp}}{\sinh \frac{\pi z_2}{sp}}\right)\right]\right)$$

$$z_1 = (x_p - x_1) + i(y_p - y_1)$$

$$z_2 = (x_p - x_2) + i(y_p - y_2)$$

It remains only to calculate σ_i and Γ_K to complete the analysis for potential flow. The purpose of using the on-body program with this program is to generate σ_i and Γ_K as the on-body program uses these values, also. The derivations and formulas for arriving at σ_i and Γ_K are spelled out in the on-body report and are far too numerous and complicated for the context of this report. Due to the use of complex numbers for cascade flow, it was not as easy to calculate the stream function analytically as with uniform flow. Therefore, unfortunately, there is no provision for plotting streamlines for cascade flow. The streamlines one obtains are those simply for the repeated configuration entered into the program, taken as if it were alone in the flow field.

References

1. Hess, J. L., and Smith, A. M. O., "Calculation of Potential Flow about Arbitrary Bodies", Progress in Aeronautical Sciences, Volume 8, D. Kuchelmann, ed., Pergamon Press, 1967, pp. 1-138.